공학박사학위논문

Coating regime maps for drying of colloidal films and convective assembly process

입자계 필름의 건조 공정과 대류자가조립 공정의 코팅 영역 지도에 관한 연구

2014년 2월

서울대학교 대학원

화학생물공학부

정 윤 동

Abstract

Coating regime maps for drying of colloidal films and convective assembly process

Yoon Dong Jung
School of Chemical and Biological Engineering
The Graduate School
Seoul National University

Particulate coatings are commonly used for many industrial products such as paints, adhesives, paper coatings, anti-reflective films, batteries, fuel cells, optical devices, data storage devices and other applications. A typical particulate coating is composed of particles, solvent, polymer binder and other additives. Although the compositions of these coatings are identical, the difference in the microstructure of the coatings established during drying is influential in the properties and performances of the final products. Therefore, it is important to understand the microstructural change during drying which can be

characterized by the particle distribution, the degree of alignment and the coating thickness. In general, as a particulate coating dries, the close-packed region is formed from the boundary of the coating. The close-packed region is the region where the particles are closely packed with the solvent filling in the interparticle void space. The capillary pressure of the meniscus in the close-packed region and the fluid flow into or through the close-packed region have a strong influence on the film formation. Therefore, predicting the formation of the close-packed region and understanding the role of the close-packed region give useful information on the microstructure such as the degree of alignment and the coating thickness as well as the particle distribution. Two particulate coating methods, drying of colloidal films and convective assembly, were investigated by modeling the formation of the close-packed region. In addition, the coating regime maps that predict the microstructural change depending on the coating conditions in terms of the dimensionless variables were created. In the case of the drying of colloidal films, the effect of evaporation, diffusion and sedimentation on the formation of the close-packed region (particle surface accumulation or sediment) was predicted by solving the particle conservation equation. From these results, the drying regime maps in terms of two

dimensionless variables, the Peclet number and the sedimentation number, were created to predict evaporation, diffusion or sedimentation dominance for a given drying conditions. The particle distribution during drying of a model system comprised of monodisperse silica particles in water was observed using cryoSEM. There was a good agreement between the experimental observations and the model predictions. In the case of the convective assembly, the role of the close-packed region in developing the colloidal crystal films was proposed, and the length of the close-packed region was predicted by solving mass balance equations. The dimensionless coating thickness as well as the dimensionless length of the close-packed region was found to be the functions of only three dimensionless variables: two capillary numbers and the initial volume fraction. From the modeling results, the coating process regime maps that predict the coating thickness for a given coating condition were created. In addition, using the model system of monodisperse silica particles in alcohol, the length of the close-packed region was measured under various coating conditions to validate the model predictions. The experiments firmly supported the model predictions.

Keywords: particulate coating, drying of colloidal films, convective

assembly, close-packed region, coating regime map, drying regime map

Student Number: 2006-21386

Contents

List of Figures

List of Tables

I. Introduction

1.1. Particulate coatings

Particulate coatings are commonly used for many industrial products such as paints, adhesives, paper coatings [Chapman 1997], anti-reflective films [Hattori 2001], batteries [Dominko et al. 2003], fuel cells [Li and Pickup 2003], solar cell [O'Regan and Gratzel 1991], biochemical sensors [Holtz and Asher 1997], optical devices [Xia et al. 2000], data storage devices [Sun et al. 2000] and other applications. Particulate coatings provide objects with functionalities such as color, durability, hydrophobicity, permeability, conductivity and anti-reflection. For example, carbon black is added to increase the electronic conductivity for batteries [Dominko et al. 2003] and fuel cells [Li and Pickup 2003], and silica particles are used to make the surface anti-reflective [Hattori 2001]. Paints and metal coatings are used to protect the surface from scratches and corrosion. In addition, by using latex coatings [Keddie and Routh 2010], it is possible

to apply a polymer onto a surface without dissolving it in organic solvents. Latex is a dispersion of polymer particles in an aqueous medium. Latex coatings are used as paints, adhesives, sealants, paper coatings, ink, latex gloves and transparent conductors. The use of water as the solvent allows latexes to be made environmentally friendly and cheaply. It is simple to control the rheology of a latex with the solid volume fraction, particle size and stability rather than by polymer composition and molecular weight. Furthermore, colloidal crystal coatings composed of monodisperse particles are used for biochemical sensors [Holtz and Asher 1997], optical devices [Xia et al. 2000] and data storage devices [Sun et al. 2000].

A typical particulate coating is composed of particles, solvent, polymer binder and other additives. Although the compositions of particulate coatings are identical, the difference in the microstructure of the films after drying is influential in the properties and performances of the final products. For example, the arrangement of carbon particles in a fuel cell electrode determines the permeability of the coating to reactive hydrogen and oxygen as well as the conductivity of the electrode [Li and Pickup 2003]. A porous particulate coating applied to paper aids in ink adsorption [Chapman 1997]. Ordered colloidal crystal coatings with photonic band gap are created by slow sedimentation [Ackerson et al. 1999; Wang et al.

2003] or evaporative assembly [Jiang et al. 1999] of monodisperse particles. The required microstructure that makes these coatings functional develops during drying. Therefore, it is important to understand the microstructural change during drying which can be characterized by the particle distribution, the degree of alignment, the porosity of particle packing and the coating thickness.

A number of modeling and experimental studies that analyzed the microstructural change of the particulate coatings have been done. Both modeling and experimental studies emphasized the formation and the role of the close-packed region. The close-packed region is the region where the particles are closely packed with the solvent filling in the interparticle void space. Routh and Zimmerman (2004) predicted the particle distribution in the vertical direction of a substrate and analyzed the formation of the close-packed region during drying by solving one-dimensional conservation equation. By applying the lubrication approximation, Routh and Russel (1998) predicted the particle distribution and the coating thickness in the horizontal direction and analyzed the close-packed region formed from the edge of the film during drying. Maki and Kumar (2011) predicted the accumulation of particles at the liquid-air interface as well as at the edge of the droplet. Deegan et al. (1997; 2000)

showed that a ring-like deposit was produced due to the capillary flow from the center to the edge of the drop induced by the differential evaporation rates across the drop. Dimitrov and Nagayama (1996) explained the role of the evaporation in the close-packed region for the convective assembly and predicted the coating thickness. Furthermore, using CryoSEM, Ma et al. (2005) observed the close-packed region in drying latex coatings. Salamanca et al. (2001) observed the movement of the boundaries of the close-packed region in the horizontal direction during drying by magnetic resonance microscopy. The movement of the boundary of the close-packed region near the meniscus was observed in the convective assembly [Dimitrov and Nagayama 1996]. Meng et al. (2006), Gasperino et al. (2008) and Brewer et al. (2008) analyzed the crystallization mechanism in the close-packed region by microscopic observation and simulations; however, the mechanism is not fully understood yet.

The capillary pressure of the meniscus in the close-packed region [Routh and Russel 1998; Salamanca et al. 2001; Dimitrov and Nagayama 1996; Fustin et al. 2004] and the fluid flow into or through the close-packed region [Fustin et al. 2004; Meng et al. 2006; Gasperino et al. 2008] have a strong influence on the film formation such as evaporation rate,

coating thickness, coffee ring effect and particle alignment. Therefore, predicting the formation of the close-packed region and understanding the role of the close-packed region give useful information on the microstructure such as the degree of alignment and the coating thickness as well as the particle distribution.

1.2. Drying of colloidal films

As a particulate coating dries, evaporation, diffusion and sedimentation influence the particle distribution. Evaporation causes the coating free surface to move towards the substrate with velocity E, increasing the particle concentration in the coating over time. (See Figure 1.1). Particles can accumulate at the descending free surface as developing the close-packed region. Thermal Brownian diffusion of particles with velocity V_D acts to eliminate concentration gradients that develop. Finally, if the particles are more dense than the surrounding medium, they can sediment with velocity U. The balance between these three motions determines whether concentration gradients develop through the coating as it dries. Concentration gradients in a drying coating often lead to property variations through the thickness of the final product and can also influence particle arrangement and packing. Concentration gradients can be undesirable, but they can also be beneficial, such as in the design of layered microstructures in coatings containing more than one type of particle.

The balance between E, V_D, and U is most usefully described through dimensionless numbers. The dimensionless Peclet number is used to describe the importance of evaporation to diffusion in a film of initial

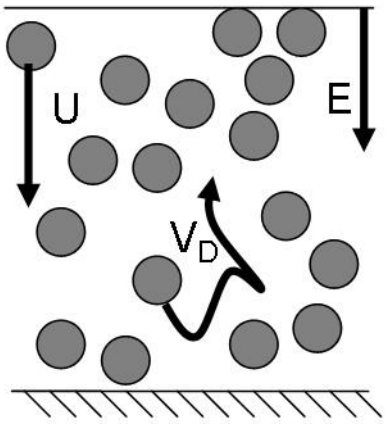

Figure 1.1. Schematic diagram showing sedimentation (U), evaporation (E) and diffusion (V_D) in a drying particulate coating.

thickness H_0 [Routh and Russel 1998]. It is given as

$$Pe = \frac{EH_o}{D_o} \tag{1.1}$$

where D_0 is the Stokes-Einstein diffusion coefficient, defined as:

$$D_0 = \frac{kT}{6\pi\mu a} \tag{1.2}$$

for a spherical particle of radius a dispersed in a liquid with viscosity μ and temperature T. The Boltzmann constant is k. Routh and Zimmerman (2004) examined the effects of evaporation with respect to diffusion using a 1D model. When evaporation is dominant ($Pe \gg 1$), the model predicts that consolidation fronts form at the air-water interface and grow in thickness as the free surface descends towards the substrate until the entire coating reaches the maximum packing fraction. When diffusion dominates ($Pe \ll 1$), the particle concentration is predicted to remain approximately uniform through the coating thickness as it dries. Similar models have been adapted to include particle charge [Sarkar and Tirumkudulu 2009] and Marangoni flows, which are common in solvent borne coatings [Yiantsios and Higgins 2006].

Limited experimental methods exist to assess the concentration gradients that develop during the active drying of coatings. The effects of varying Pe on particle distributions in coatings have been studied experimentally using magnetic resonance (MR) profiling, which can be used to track concentrations of water in a drying film to a resolution of about $10\,\mu m$ [Gorce et al. 2002; Ciampi et al. 2000]. This technique confirmed predictions that water concentration gradients occur in a drying film when $Pe > 1$. Specifically, MR profiling confirmed theoretical predictions that the water concentration gradient between the consolidation front and the bulk of the film scales with $Pe^{1/2}$ [Ekanayake et al. 2007]. Raman spectroscopy is another experimental technique able to obtain concentration profiles in real time, as long as the coating is relatively clear and the species are Raman active [Schabel et al. 2004]. Cryogenic scanning electron microscopy (cryoSEM) has also been successfully used to image consolidation front growth in particulate coatings [Ma et al. 2005]. By vitrifying the coating in liquid ethane before it is completely dry, the microstructure of the coating can be frozen in time and imaged in a scanning electron microscope on a temperature-controlled stage. By imaging specimens frozen after different extents of drying, the developing microstructure can be characterized. In this way,

Luo et al. (2008) studied the effects of varying drying rate on the microstructure formation of a large latex/small silica blend. Since these MR and cryoSEM studies were primarily focused on predicting the particle distribution of latex coatings, the effects of sedimentation were ignored.

The first model describing the sedimentation of particles was formulated by Kynch (1952), who showed that there are three main regions in a sedimenting suspension: the sediment near the bottom, a region where the concentration equals the initial concentration, and a particle free-zone at the top. This model has been adapted for colloidal systems that experience diffusion [Buscall and White 1987; Davis and Russel 1989]. The strength of sedimentation is compared to diffusion using the sedimentation Peclet number,

$$Pe_{sed} = \frac{U_o H_o}{D_o} \tag{1.3}$$

where U_0 is the Stokes settling velocity of a spherical particle of density ρ_p in a dilute solution of liquid with density ρ and viscosity μ, under gravitational acceleration g:

$$U_0 = \frac{2a^2 g\left(\rho_p - \rho\right)}{9\mu} \tag{1.4}$$

Increasing the strength of diffusion (decreasing Pe_{sed}) softens the boundaries between the three concentration regions. Various researchers have experimentally observed the effects of varying Pe_{sed} on the sedimentation of colloidal suspensions over centimeter sized distances in the absence of evaporation using techniques such as light extinction [Davis and Birdsell 1988], X-ray tomography [Davis et al. 1991], and light scattering [van Duijneveldt et al. 1993]. Experiments agreed well with models.

The sedimentation number, N_s, is used to describe the strength of sedimentation to evaporation.

$$N_s = \frac{U_o}{E} = \frac{Pe_{sed}}{Pe}. \tag{1.5}$$

Although the effects of varying Pe and Pe_{sed} have been studied independently, sedimentation, diffusion and evaporation have not yet been studied together for coating systems. Because many researchers do not have the means to observe coating microstructure during drying, the path of the microstructure development is often indirectly inferred from final

coating appearance rather than designed intelligently.

1.3. Convective assembly

Convective assembly is a coating method to fabricate thin films with ordered particle structures which can be used extensively for biochemical sensors, data storage devices, optical devices and other applications. The general procedure is shown in Figure 1.2. By placing or lifting slowly a nearly vertical substrate in the bath of a dilute suspension during drying, a thin film with an ordered particle structure develops [Fustin et al. 2004; Jiang et al. 1999; Marlow et al. 2009]. It may well be considered as the dip coating of a dilute suspension at a very low processing speed. In analyzing the dip coating process, capillary number Ca defined as the relative strength between the viscous stress and the capillary pressure is important.

$$Ca = \frac{\mu(E + u_s)}{\gamma} \tag{1.6}$$

Here, μ is the solvent viscosity, γ is the solvent surface tension, E is the evaporation rate and u_s is the drawing speed (E has the same unit as u_s). For convenience, the properties of the dilute suspension was assumed to be the same as the properties of the solvent. Ca_0 is Ca when the drawing speed is zero. In this article, a low processing speed means that

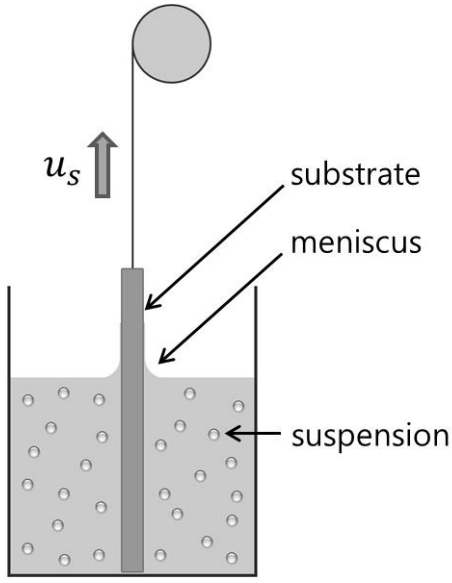

Figure 1.2. Schematic of the convective assembly.

Ca is small and a high processing speed means that Ca is large.

For a large Ca, the viscous stress, which is induced by the movement of the substrate, dominates the dip coating process. This corresponds to the typical dip coating process condition, and the wet coating thickness is determined by the well-known Landau-Levich equation [Landau and Levich 1942]. During drying, the particle volume fraction of the film developed by the Landau-Levich deposition increases from the initial volume fraction, ϕ_0, to the particle volume fraction of the random close packing structure, $\phi_r = 0.64$. The dry coating thickness, $h_{LL,dry}$, is the wet coating thickness, $0.945 l_c Ca^{2/3}$, multiplied by $\phi_0/0.64$ as follows:

$$\frac{h_{LL,dry}}{l_c} = 1.48 Ca^{2/3} \phi_0, \tag{1.7}$$

where $l_c = \sqrt{\gamma/\rho g}$ is the capillary length which represents the height of the capillary rise (ρ is the solvent density and g is the acceleration of the gravity). As Ca increases, the coating thickness increases in proportion to $Ca^{2/3}$. Ouriemi and Homsy (2013) and Dixit and Homsy (2013) found that presence of surface-adsorbed hydrophobic particles results in a slightly different power law from the Landau-Levich equation. However, the effect of interfacial elasticity was neglected in this work.

For the convective assembly to develop a well-ordered structure, the particle volume fraction after drying was assumed to be the particle volume fraction of the close-packed lattice structure, $\phi_m = 0.74$. In the Landau-Levich deposition which cannot develop 3-dimensional close-packed lattice structure as in the convective assembly, the particle volume fraction after drying is less than 0.74 [Routh and Russel 1998; Russel 1990]. Here, we assumed a random close packing at $\phi_r = 0.64$ [Routh and Russel 1998; Routh and Zimmerman 2004].

For a small Ca, the film is formed by the convective assembly. Figure 1.3 shows the idealized view of the close-packed region explaining the mechanism of the convective assembly. The particle packing front is the lower boundary of the close-packed region, and drying front is the upper boundary of the close-packed region. The wet coating thickness, which is the thickness of the close-packed region, equals the coating thickness of the dry film located above the drying front. l_0 and h_0 represent the length of the close-packed region and the coating thickness of the convective assembly, respectively. When Ca is small enough, the close-packed region is formed on the substrate near the meniscus at the early stage of drying and the fluid flow into or through the close-packed region due to evaporation in the close-packed region causes the convective

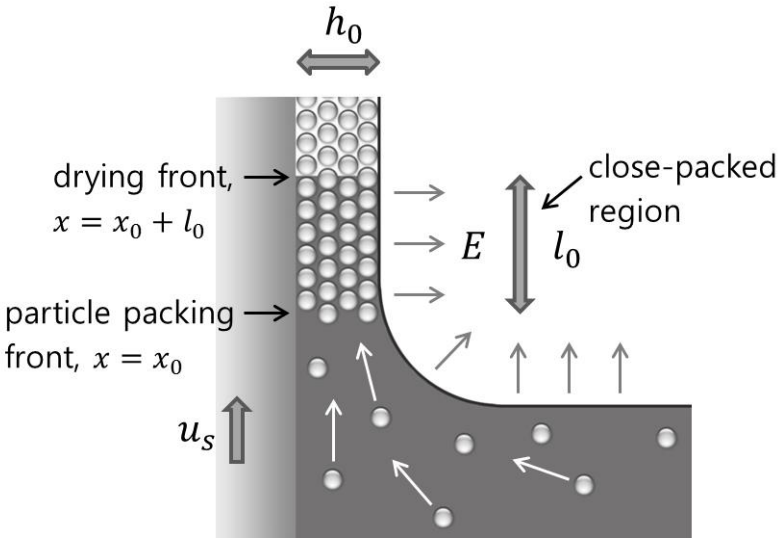

Figure 1.3. Idealized view of the close-packed region.

assembly. Therefore, the coating thickness of the convective assembly is mainly affected by the evaporation in the close-packed region, not the viscous stress.

Le Berre et al. (2009), Brewer et al. (2011) and Berteloot et al. (2012) measured the coating thickness of the dip coating of colloidal suspensions in a wide range of Ca from the convective assembly to the Landau-Levich deposition. They showed that the coating thickness decreases as Ca increases at the small Ca region where the film is formed by the convective assembly, while the coating thickness increases with Ca at the large Ca region where the film is formed by the Landau-Levich deposition.

To predict the coating thickness of the convective assembly, it is important to estimate the length of the close-packed region. Dimitrov and Nagayama (1996) explained the role of evaporation in the close-packed region and predicted the coating thickness. Berteloot et al. (2012) predicted the coating thickness using the scale of the meniscus size. However, an accurate prediction could not be made because the length of the close-packed region was either assumed to be constant or neglected. The coating thickness of the convective assembly was measured

experimentally under various coating conditions [Fustin et al. 2004; Jiang et al. 1999; Vlasov et al. 2001; Zhou and Zhao 2004; Im et al. 2003], but there have been few attempts to observe the length of the close-packed region as a function of the coating conditions.

II. Theory

2.1. Drying of colloidal films

The particle volume fraction as a function of position and time within a drying coating containing a volatile liquid and particles is obtained by solving the particle conservation equation, adapted from Russel and coworkers [Russel et al. 1989]. When the coating thickness is small relative to its lateral dimensions, the drying of a particulate coating is assumed to be a one dimensional process. The 1D conservation equation describing the particle volume concentration (ϕ) in a particulate coating during the drying process, including diffusion, evaporation, and sedimentation, is expressed as:

$$\frac{\partial \phi}{\partial t} = \frac{\partial}{\partial y}\left(U\phi + D\frac{\partial \phi}{\partial y} \right). \qquad (2.1)$$

A no-flux boundary condition is applied at the substrate ($y = 0$). At the top surface ($y = H_0 - Et$) there is an effective particle flux into the coating due to evaporation:

$$U\phi + D\frac{\partial \phi}{\partial y} = 0 \qquad at\ y = 0 \qquad (2.2)$$

$$U\phi + D\frac{\partial \phi}{\partial y} = E\phi \qquad y = H_o - Et \qquad (2.3)$$

where H_0 is the initial coating thickness, E is the evaporation rate given in terms of free surface velocity, D is the particle mutual diffusion coefficient and U is the particulate sedimentation velocity.

The effect of particle concentration on E is negligible [Routh and Russel 1998]. The effects of particle concentration on D and U are described through the sedimentation coefficient, $K(\phi)$, which describes hydrodynamic interactions, and the compressibility factor, $Z(\phi)$, which represents the concentration dependence of the osmotic pressure gradient for hard sphere particles. Both parameters are strong functions of ϕ.

$$D(\phi) = K(\phi)\frac{d}{d\phi}\left[\phi Z(\phi)\right]D_0, \quad D_0 = \frac{kT}{6\pi\mu a} \qquad (2.4)$$

$$U(\phi) = K(\phi)U_0, \qquad U_0 = \frac{2a^2 g\left(\rho_p - \rho\right)}{9\mu}. \qquad (2.5)$$

The sedimentation coefficient $K(\phi)$ has a functional form $K(\phi) =$

$(1-\phi)^{6.55}$ [Russel et al. 1989]. This equation was shown experimentally to satisfactorily represent the dependence of sedimentation speed on concentration for the model system. The compressibility factor, $Z(\phi)$, takes the general form [Russel et al. 1989; Routh and Zimmerman 2004] $Z(\phi)=\frac{1}{(\phi_{max}-\phi)}$ where ϕ_{max} is the maximum value of ϕ. This form of compressibility factor captures the divergence of the diffusion coefficient near the particle maximum packing fraction due to increased particle collisions and maintains appropriate values near the dilute limit. The maximum packing fraction was chosen to be $\phi_{max}=0.64$, assuming random close packing of the particles. Both the sedimentation coefficient and the compressibility factor assume that the particles interact as hard spheres.

The conservation equation is nondimensionalized with

$$\bar{t}=\frac{t}{H_o/E} \quad and \quad \bar{y}=\frac{y}{H_o}. \tag{2.6}$$

$$\frac{\partial\phi}{\partial\bar{t}}=\frac{\partial}{\partial\bar{y}}\left[N_s K(\phi)\phi+\frac{1}{Pe}K(\phi)\frac{d}{d\phi}\left[\phi Z(\phi)\right]\frac{\partial\phi}{\partial\bar{y}}\right] \tag{2.7}$$

$$N_s K(\phi)\phi + \frac{1}{Pe} K(\phi) \frac{d}{d\phi}\left[\phi Z(\phi)\right] \frac{\partial \phi}{\partial \bar{y}} = 0 \qquad at\ \bar{y} = 0 \qquad (2.8)$$

$$N_s K(\phi)\phi + \frac{1}{Pe} K(\phi) \frac{d}{d\phi}\left[\phi Z(\phi)\right] \frac{\partial \phi}{\partial \bar{y}} = \phi \qquad at\ \bar{y} = 1 - \bar{t} \qquad (2.9)$$

Nondimensionalization reveals the two main dimensionless variables discussed in this report, Pe and N_s. These equations are valid up to the time when the entire coating is packed with maximum packing ϕ_{max}. This dimensionless time, $\bar{t}_m$, is given by:

$$\bar{t}_m = \frac{\phi_{\max} - \phi_o}{\phi_{\max}}. \qquad (2.10)$$

A shrinking coordinate system with a dimensionless shrinking velocity of 1 was used to fix the free surface boundary. The shrinking space and time coordinates are defined by:

$$\xi = \frac{\bar{y}}{1 - \bar{t}}, \quad \tau = \bar{t}. \qquad (2.11)$$

The dimensionless conservation equation and boundary conditions in the shrinking coordinate system are:

$$\frac{\partial \phi}{\partial \tau} + \frac{\xi}{1-\tau}\frac{\partial \phi}{\partial \xi} = \frac{N_s}{(1-\tau)}\frac{\partial}{\partial \xi}\left[K(\phi)\phi\right] + \frac{1}{Pe(1-\tau)^2}\frac{\partial}{\partial \xi}\left[K(\phi)\frac{d}{d\phi}\left[\phi Z(\phi)\right]\frac{\partial \phi}{\partial \xi}\right] \tag{2.12}$$

$$N_s Pe\phi(1-\tau) + \frac{d}{d\phi}\left[\phi Z(\phi)\right]\frac{\partial \phi}{\partial \xi} = 0 \qquad at\ \xi = 0 \tag{2.13}$$

$$N_s PeK(\phi)\phi(1-\tau) + K(\phi)\frac{d}{d\phi}\left[\phi Z(\phi)\right]\frac{\partial \phi}{\partial \xi} = Pe(1-\tau)\phi \qquad at\ \xi = 1\ . \tag{2.14}$$

Equations 12-14 describe the particle distribution before the liquid recedes into the packed particles. After the liquid enters the packing, capillary effects must be taken into account. These effects and their implications on the structure of packings of deformable particles have been modeled by Routh and Russel (1999). Specifically, they have created a process map that identifies conditions when a packed particle layer at the free surface deforms into a dense skin.

2.2. Convective assembly

It is important to predict the length of the close-packed region in order to understand the convective assembly process. As the solvent flows through the close-packed region and experiences a pressure drop, the flow can be described by Darcy's law. Then the length of the close-packed region and the coating thickness can be obtained by solving the particle balance equation, the solvent balance equations and Darcy's law in the close-packed region.

To model l_0 and h_0, several assumptions were required. First, evaporation in the close-packed region was assumed to have a strong influence on the film formation. The validity of this assumption was demonstrated in the discussion on the mechanism of the convective assembly in Figure 1.3. Second, because h_0 is small relative to the substrate width, the edge effect was neglected. Third, the pressure drop by gravity was assumed to be negligible. In the close-packed region, the maximum capillary pressure of the spherical-cap meniscus in the pore within the close-packed particles of radius a is approximated as $10\gamma/a = 2.2\,MPa$, with $a = 100\,nm$ for alcohol [Brown 1956]. This pressure is equivalent to the pressure drop caused solely by gravity with

the height of a column of solvent being $290\,m$, which is much larger than the length scale ($\sim mm$) of the close-packed region in the experiments. So the pressure drop by gravity can be neglected in the convective assembly with the particle size being smaller than or equal to several micrometers. Fourth, the effect of the particle volume fraction on the evaporation rate was negligible because the presence of the particles, which are much bigger than the solvent molecules, hardly affects the solvent vapor pressure [Routh and Russel 1998]. Fifth, the particle volume fraction was assumed to be uniform in the bath during drying because the size of the bath is large relative to that of the coated film. Sixth, h_0 was assumed to have a continuous value in the modeling, though the film has a discontinuous coating thickness because it forms layers of the close-packed particles. And the particles were assumed to be monodisperse hard spheres.

By equating the volumetric flow rate of the particle from the bulk solution into the particle packing front and the rate of particle accumulation, the particle balance equation at the particle packing front, $x = x_0$, can be established.

$$\phi_0 h_0 w \bar{u}_x(x_0^-) = (\phi_m - \phi_0) h_0 w (E + u_s) \tag{2.15}$$

The *x*-axis is parallel to the substrate. x_0 is the position of the particle packing front and $x_0 + l_0$ is the position of the drying front. x_0^- is the position beneath the particle packing front and x_0^+ is the position above the particle packing front. w is the width of the substrate. The particle volume fraction in the close-packed region equals ϕ_m because the particles form a close-packed lattice structure in the close-packed region. $\bar{u}_x$ is the flow rate of the fluid in the *x*-direction averaged over the film thickness. $\bar{u}_x$ is the flow rate of the solution below the close-packed region and becomes the flow rate of the solvent in the close-packed region where the particle movement is restrained. $\bar{u}_x(x_0^-)$ is the flow rate of the solution beneath the particle packing front. On the right hand side of Eq. 2.15, the particles are accumulated at the particle packing front at a rate of $E + u_s$ because the substrate is drawn at a rate of u_s and the level of the coating solution descends at the rate of E by evaporation. Then an expression for $\bar{u}_x(x_0^-)$ can be obtained as follows:

$$\bar{u}_x(x_0^-) = \frac{(\phi_m - \phi_0)}{\phi_0}(E + u_s). \qquad (2.16)$$

By equating the volumetric flow rate of the solvent from the bulk solution into the particle packing front and the difference between the

volumetric flow rate of the solvent from the particle packing front toward the close-packed region and the rate of reduction of the solvent due to the descent of the particle packing front, the solvent balance equation at the particle packing front, $x = x_0$, can be set up as follows:

$$(1-\phi_0)h_0 w\bar{u}_x(x_0^-) = (1-\phi_m)h_0 w\bar{u}_x(x_0^+) - (\phi_m - \phi_0)h_0 w(E+u_s)\,, \tag{2.17}$$

where $\bar{u}_x(x_0^+)$ is the flow rate of the solvent above the particle packing front. After utilizing $\bar{u}_x(x_0^-)$ from Eq. 2.16 in Eq. 2.17, $\bar{u}_x(x_0^+)$ can be derived as follows:

$$\bar{u}_x(x_0^+) = \frac{(\phi_m - \phi_0)}{(1-\phi_m)\phi_0}(E+u_s)\,. \tag{2.18}$$

When the volume of the solvent evaporation in the close-packed region is approximated as being equal to the volumetric flow rate of the solvent right above the particle packing front, the solvent balance equation in the closed-packed region, $x_0 < x < x_0 + l_0$, can be established.

$$l_0 wE = (1-\phi_m)h_0 w\bar{u}_x(x_0^+) \tag{2.19}$$

Then h_0 in Eq. 2.19 can be solved using $\bar{u}_x(x_0^+)$ from Eq. 2.18.

$$h_0 = \frac{\phi_0}{(\phi_m - \phi_0)(1+\frac{u_s}{E})} l_0 . \quad (2.20)$$

Assuming ϕ_0 is small and substituting 0.74 for ϕ_m, the following can be obtained.

$$h_0 = 1.35 \frac{\phi_0}{(1+\frac{u_s}{E})} l_0 \quad (2.21)$$

Dimitrov and Nagayama (1996) obtained the coating thickness of the convective assembly as follows:

$$n = \frac{\beta l_0 E \phi_0}{1.21 a v_c^{(n)} (1-\phi_0)}, \quad (2.22)$$

where n is the number of layers; β is the ratio between the velocity of a particle in solution and the fluid velocity and $v_c^{(n)}$ is the growth rate of the n-layer array. As the particles form the close-packed lattice structure in the close-packed region, the coating thickness can be expressed as $h_0 = \frac{2\sqrt{6}}{3} na + \left(2 - \frac{2\sqrt{6}}{3}\right) a$. Assuming $h_0 \gg \left(2 - \frac{2\sqrt{6}}{3}\right) a$, h_0 is approximated as $\frac{2\sqrt{6}}{3} na$. After substituting $E + u_s$ for $v_c^{(n)}$, 1 for β and $\frac{2\sqrt{6}}{3} na$ for h_0 in Eq. 2.22 and assuming ϕ_0 is small, the same

result with Eq. 2.21 can be obtained. l_0 is included in both Eq. 2.21 and Eq. 2.22. However, l_0 is not a constant and needs to be a function of the material properties and coating conditions.

The solvent flow through the close-packed region can be described by Darcy's law. l_0 can be modeled by equating the amount of pressure drop in the close-packed region calculated by Darcy's law and the maximum capillary pressure of the spherical-cap meniscus in the pore of the close-packed region.

The flow rate of the solvent in the closed-packed region, $x_0 < x < x_0 + l_0$, can be obtained from the continuity equation of the solvent. By equating the divergence of the volumetric flow rate of the solvent and the evaporation rate of the solvent, the continuity equation of the solvent in the close-packed region can be derived.

$$\frac{\partial}{\partial x}\left[(1-\phi_m)h_0 w\bar{u}_x(x)\right] = -wE \tag{2.23}$$

Because the flow rate of the solvent is expressed by Eq. 2.18 above the particle packing front and is zero at the drying front, the boundary conditions on Eq. 2.23 are

$$\bar{u}_x = \frac{(\phi_m - \phi_0)}{(1-\phi_m)\phi_0}(E + u_s) \qquad at\ x = x_0^+ \tag{2.24}$$

$$\bar{u}_x = 0 \qquad at\ x = x_0 + l_0. \tag{2.25}$$

Then $\bar{u}_x(x)$ becomes

$$\bar{u}_x(x) = \frac{(E + u_s)(\phi_m - \phi_0)}{(1-\phi_m)\phi_0}\left[1 - \frac{(x - x_0)}{l_0}\right]. \tag{2.26}$$

The solvent flow through the close-packed region is described by Darcy's law, adapted from Routh and Russel (1998). Because in the close-packed region Reynolds number, $Re = \frac{\rho \bar{u}_x a}{\mu}$, is on the order of 10^{-6} with $E = 10^{-7}\ m/s$ and $a = 100\ nm$, it is valid to apply Darcy's law.

$$\frac{\partial p}{\partial x} = -\frac{\mu}{k_p}(1-\phi_m)\left(\bar{u}_x - u_s\right) = -\frac{75\mu\phi_m{}^2}{2a^2(1-\phi_m)^2}\left(\bar{u}_x - u_s\right), \tag{2.27}$$

where p is the pressure and k_p is the permeability. k_p is the function of ϕ_m and a according to the Carman-Kozeny equation [Carman 1937]. Because the capillary pressure has a maximum value at $x = x_0 + l_p$ where the pressure gradient becomes zero and the maximum capillary pressure of the meniscus in the close-packed region can be approximated

as $10\gamma/a$,

$$p_c(x_0 + l_p) \approx \frac{10\gamma}{a}, \tag{2.28}$$

where p_c is the capillary pressure, and l_p is the length between the particle packing front and the position where the pressure gradient is zero in the close-packed region. According to Eq. 2.27, the flow rate of the solvent equals u_s at the position where the pressure gradient is zero. By substituting $x = x_0 + l_p$ and $\bar{u}_x = u_s$ into Eq. 2.26, l_p/l_0 can be obtained.

$$\frac{l_p}{l_0} = 1 - \frac{(1-\phi_m)\phi_0}{(\phi_m - \phi_0)\left(1 + \frac{E}{u_s}\right)} \tag{2.29}$$

If ϕ_0 is small, the second term of the right hand side is negligible and l_p is approximately equal to l_0. So the maximum capillary pressure appears near the drying font. By equating the amount of the pressure drop calculated by integrating Eq. 2.27 from $x = x_0$ to $x = x_0 + l_p$ after using $\bar{u}_x(x)$ from Eq. 2.26 into Eq. 2.27 and the maximum capillary pressure, the following equation is obtained.

$$-\int_{x_0}^{x_0+l_p} -\frac{75\mu\phi_m{}^2}{2a^2(1-\phi_m)^2}\left\{\frac{(E+u_s)(\phi_m-\phi_0)}{(1-\phi_m)\phi_0}\left[1-\frac{(x-x_0)}{l_0}\right]-u_s\right\}dx=\frac{10\gamma}{a} \quad (2.30)$$

By solving both Eq. 2.29 and Eq. 2.30, the following equation is derived:

$$l_0=\frac{8a\gamma(1-\phi_m)^3}{15\mu E\left(1+\frac{u_s}{E}\right)\phi_m{}^2\left[1-\frac{(1-\phi_m)\phi_0}{(\phi_m-\phi_0)(1+\frac{E}{u_s})}\right]^2}\frac{\phi_0}{(\phi_m-\phi_0)}. \quad (2.31)$$

Finally, after inserting l_0 in Eq. 2.31 into Eq. 2.20, h_0 is obtained as a function of the material properties and the coating conditions.

$$h_0=\frac{8a\gamma(1-\phi_m)^3}{15\mu E\left(1+\frac{u_s}{E}\right)^2\phi_m{}^2\left[1-\frac{(1-\phi_m)\phi_0}{(\phi_m-\phi_0)(1+\frac{E}{u_s})}\right]^2}\frac{\phi_0{}^2}{(\phi_m-\phi_0)^2} \quad (2.32)$$

If ϕ_0 is small, the dimensionless length of the close-packed region and the dimensionless coating thickness can be expressed simply as functions of three dimensionless variables: Ca, Ca_0 and ϕ_0.

$$\frac{l_0}{a} = 0.023 \frac{\gamma}{\mu(u_s + E)} \phi_0 = 0.023 Ca^{-1} \phi_0 \tag{2.33}$$

$$\frac{h_0}{a} = 0.031 \frac{\gamma E}{\mu(u_s + E)^2} \phi_0{}^2 = 0.031 Ca_0 Ca^{-2} \phi_0{}^2 \tag{2.34}$$

When $u_s = 0$, Eq. 34 yields

$$\frac{h_0}{a} = 0.031 Ca_0{}^{-1} \phi_0{}^2 . \tag{2.35}$$

III. Methods

3.1. Drying of colloidal films

3.1.1. Numerical method

The dimensionless conservation equation in shrinking coordinates was solved numerically using COMSOL Multiphysics 3.2. The PDE General Form Application Mode with Direct (UMFPACK) Linear system solver was used. The model has 480 elements and a 10^{-5} time step size that gave sufficient accuracy for most cases. Other settings were the default values of COMSOL. Two limiting cases of the conservation equation were verified with known numerical solutions: the distribution of particles during solvent evaporation from coatings [Routh and Zimmerman 2004], and an asymptotic description of transient settling and ultrafiltration of colloidal dispersions [Davis and Russel 1989].

3.1.2. Experimental methods

A model system of monodisperse silica particles in water was used for an experimental comparison to the theoretical model. Monodisperse silica particles with diameters ranging from $200\,nm$ to $1\,\mu m$ were synthesized using the Stober method [Stöber et al. 1968; Bogush et al. 1988]. Particles were washed after synthesis and suspended in distilled water at $\mathrm{pH}\,10$ with various initial volume fractions. The density of the particles was measured through water displacement to be $1.9\,g/cm^3$. Additionally, monodisperse silica particles of $1\,\mu m \pm 1.5\%$ diameter (Monosphere, Merck) and density of $2.2\,g/cm^3$ were also used.

Controlled volumes of coating suspension were spread on $5 \times 7\,mm$ silicon substrates using a micropipette and samples were allowed to dry for various times in still air or under forced air. By controlling the drying environment, the evaporation rate, E, could be varied from 1.5 to $100\,\mu m/min$. Drying rates were determined by measuring the coating thickness over time from cryoSEM images.

The particle distribution within the coatings was imaged using cryoSEM. After samples had dried for various amounts of time, the coatings were plunged into liquid ethane at $-196\,℃$ for vitrification.

Samples were then transferred to an Emitech K-1250 cryo preparation chamber where they were fractured at $-120\,℃$ under liquid nitrogen to expose the coating cross-section, sublimed at $-96\,℃$ for 5-7 minutes to reveal the particles and sputter coated with a $2\,nm$ layer of platinum to reduce charging in the electron microscope. Finally, samples were imaged in a Hitachi S4700 FESEM at $-160\,℃$. In most cases, samples dried edge-in as well as top-down; therefore, all data and images were taken as close to the middle of the coating as possible.

3.2. Convective assembly

3.2.1. Experimental methods

A model system of monodisperse silica particles in alcohol was used to compare the modeling results to the experiments. While keeping the substrate fixed, the length of the close-packed region, l_0, was measured under various coating conditions with different initial volume fraction, ϕ_0, and evaporation rate, E.

Monodisperse silica particles of $200\,nm \pm 7\%$ in diameter were synthesized using the Stober method [Stöber et al. 1968; Bogush et al. 1988]. The particles were suspended in alcohol. Figure 3.1 shows the schematic of the experimental setup. $18\,ml$ of coating solution were added in a $30 \times 30 \times 30\,mm$ glass cell and dried in a sealed box at 22 ℃. Sealed boxes of different sizes, $8\,L$, $40\,L$ and $150\,L$, were used to control the evaporation rate. Because the experiments were performed only for $u_s = 0$, the inner wall of the glass cell could be substituted for the substrate. While the particles were being coated on the inner wall of the glass cell, l_0 was measured by taking the images of the wall using a CCD camera. Because the solution concentration in the glass cell increases as drying proceeds, l_0 was measured when the free surface

descended to an equal length of $5\,mm$. E was determined by measuring the level of the free surface from the images.

Figure 3.2 shows the image of the inner wall of the glass cell with a black background. The close-packed region looks substantially transparent because it is a thin film with solvent filled in the interparticle void space. A dried film (white color) is formed above the close-packed region. Below the close-packed region, the coating solution in the glass cell looks white. So the black area between the two white areas is the close-packed region. The upper boundary of the black area is the drying front and the lower boundary is the particle packing front.

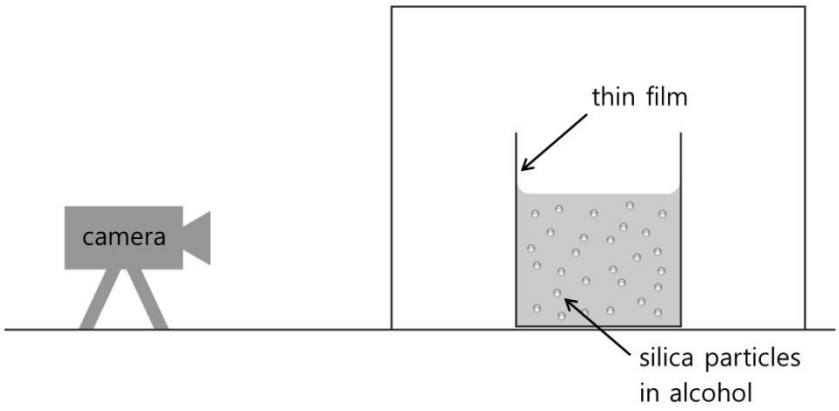

Figure 3.1. Schematic of the experimental setup.

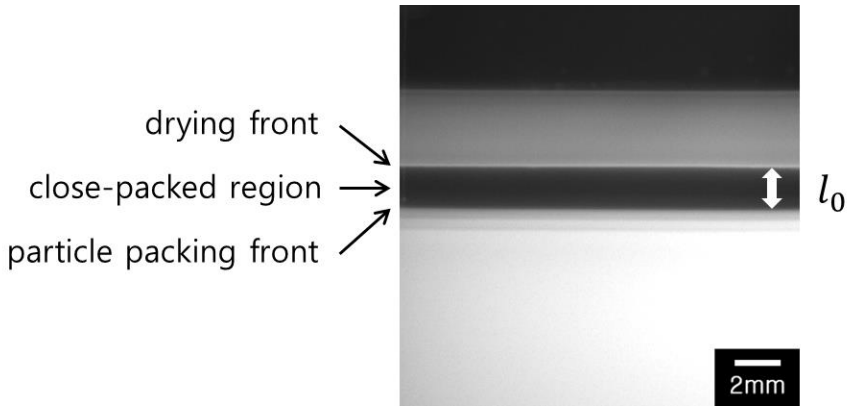

Figure 3.2. Image of the close-packed region.

IV. Results and Discussion

4.1. Drying of colloidal films

4.1.1. Numerical results

Figure 4.1 shows particle concentration profiles calculated based on Eq. 2.12 for Pe ranging from 0.1 to 10 and N_s ranging from 1 to 100 with $\phi_0 = 0.4$. As the coating dries, the coating thickness reduces and the particle volume fraction approaches the maximum packing fraction, $\phi_{max} = 0.64$, at long drying times. At intermediate times, the concentration profile within the coating is significantly affected by the relative magnitudes of N_s and Pe. Two main cases are discussed here: low N_s, where the tendency for sedimentation is small relative to evaporation and high N_s where sedimentation overwhelms evaporation.

At low N_s, ($N_s = 1$) where sedimentation is weak, the concentration profile through the depth of the coating reflects the competition between evaporation and diffusion. This competition is described by Pe. Increasing Pe, which corresponds to increasing evaporation rate, coating

thickness, or particle radius, increases the importance of evaporation on particle distribution. In an evaporation dominant coating, the suspension-air free surface descends quickly towards the substrate faster than particles can diffuse away. Consequently, particles accumulate at the free surface in a drying front. As evaporation proceeds, the coating thickness shrinks and the thickness of the front grows towards the substrate until the entire coating is at the maximum packing fraction. These results concur with previous researchers [Routh and Russel 1998]. Conversely, at low N_s and low Pe, diffusion dominates over evaporation and the particle concentration remains homogeneous through the depth of the coating as it dries.

At high N_s, ($N_s = 100$) where evaporation is slow, the concentration profile is determined by a competition between sedimentation and diffusion. At high Pe, where sedimentation is strongest, particles fall towards the substrate faster than the free-surface descends, creating a particle-free zone near the air-suspension interface. Particles accumulate at the substrate, and the resulting concentration slows their speed of descent according to Eq. 2.5. Also, the strength of diffusion is increased dramatically at concentrations approaching the maximum packing fraction, reflecting the sediment compressibility [Buscall and White 1987; Davis

and Russel 1989]. These two factors create a transition region of gradually increasing concentration between the initial-concentration zone and the sediment. This phenomenon is stronger at lower Pe, where the diffusion coefficient and its dependence on concentration are significant. At very low Pe, just as in the low N_s case, diffusion is strong and the particle concentration is uniform through the coating thickness throughout the drying. These results also agree with previous work [Davis and Russel 1989].

At intermediate N_s values, sedimentation and evaporation behaviors are both important in the drying of the coating. Particles concentrate at the top and the bottom of the coating, while the center remains near the initial volume fraction of particles. Increasing the strength of sedimentation (increasing N_s) at a constant Pe decreases the rate of particle accumulation at the top surface by creating a downward flux of particles.

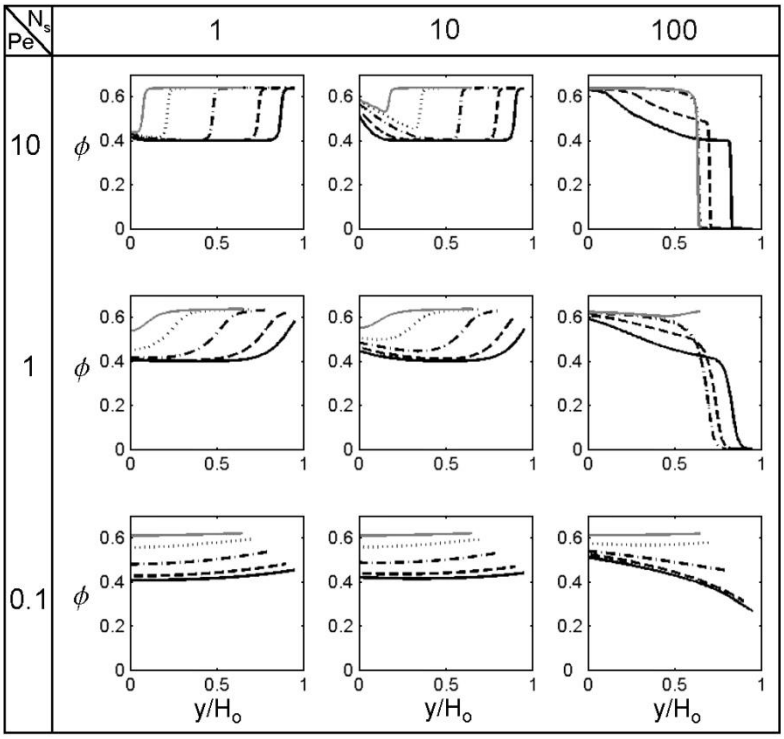

Figure 4.1. Particle volume fraction (ϕ) profiles for various N_s and Pe with respect to the fixed coordinate y/H_0 at various dimensionless times: $\bar{t} = 0.05$ (—), $\bar{t} = 0.1$ (---), $\bar{t} = 0.2$ (-.-.), $\bar{t} = 0.3$ (....), and $\bar{t} = 0.35$ (—). Initial volume fraction: $\phi_0 = 0.4$.

4.1.2. Drying regime maps

Drying regime maps - *$logH_o$ vs. logE*

To understand the effects of changing, the process conditions on the drying behavior, drying maps were created to predict evaporation, sedimentation or diffusion dominance for a given initial coating thickness and evaporation rate. These maps were inspired by the work of Cairncross et al (1996) on the drying regime maps for sol-gel coatings. In Figures 4.2 and 4.3, the black lines represent the conditions where the local particle concentration at the top or the bottom of the coating reaches 90% of the maximum packing fraction in less than half the time required for the entire coating to reach that concentration.

$$\phi\left(\xi = 0, \bar{t} = \frac{\bar{t}_m}{2}\right) \geq 0.9\phi_{\max} \qquad \text{Sediment} \qquad (4.1a)$$

$$\phi\left(\xi = 1, \bar{t} = \frac{\bar{t}_m}{2}\right) \geq 0.9\phi_{\max} \qquad \text{Skin} \qquad (4.1b)$$

When this accumulation, which is also termed a “close-packed region”, occurs at the top of the coating, evaporation dominates and the region of the map that borders this condition is called the “evaporation regime” and is labeled “E”. In this thesis, top surface particle accumulation is termed a

"skin" although the influence of particle accumulation on the evaporation rate is not modeled. Not surprisingly, evaporation tends to dominate for coatings dried at higher rates. Particle accumulation at the base forms a "sediment", which defines the "sedimentation" drying regime ("S"). Sedimentation is found at increased coating thickness, where particles have more time to sediment before the overall particle concentration reaches the maximum packing fraction. At relatively low evaporation rates, the diffusion of particles is the dominant motion in the coating; this region is the diffusion drying regime ("D"). At limited conditions, the evaporation and sedimentation regions overlap, indicating that accumulation occur at both the top and the bottom of the coating as it dries.

Figure 4.2 shows the effect of initial volume fraction in the coating dispersion. As the initial volume fraction decreases, hydrodynamic and particle interactions decrease and speed the sedimentation and diffusion rates. Using the current model, diffusion rates are approximately twice as fast at $\phi_0 = 0.1$ than at $\phi_0 = 0.3$, meaning that higher evaporation rates are necessary to promote skin formation in less concentrated coatings. Also, decreased particle concentration corresponds to a decreased number of particles that are accumulated at the coating surface for a given amount

of evaporation. Similarly, the boundary between sedimentation and diffusion is shifted to increase the size of the diffusion regime at lower particle concentrations, although the overall shape of the boundaries is retained.

Figure 4.3 compares the drying regimes for coatings containing particles of different sizes. As particle radius increases, the sedimentation rate increases, and sediments form before the entire coating reaches a maximum packing in thinner coatings. As particle radius increases, the strength of diffusion decreases, so at lower evaporation rates skins can form.

Figures 4.2 and 4.3 display data comparing individual coating systems and provide an intuitive basis for the drying regimes. However, it would also be useful to have a universal drying map to predict the behavior for a wide variety of coating formulations and conditions.

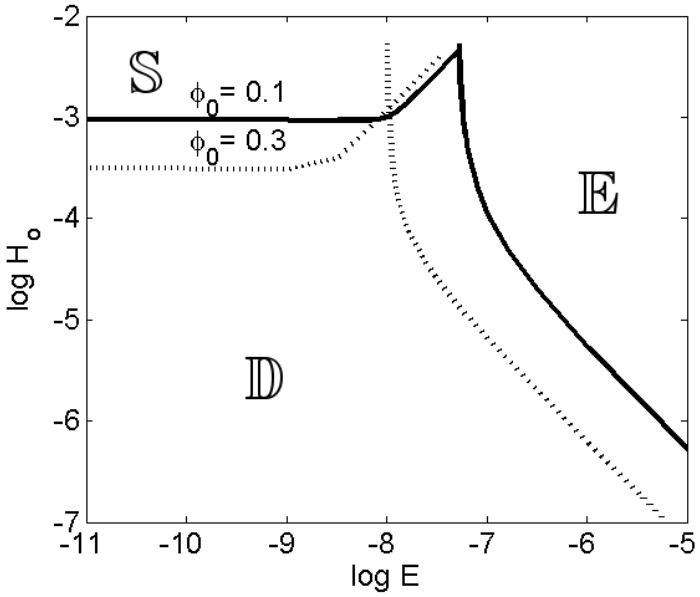

Figure 4.2. Drying regime map based on dimensional coordinates: initial coating thickness $H_0\,[m]$ and evaporation rate $E\,[m/s]$. The effect of initial particle volume fraction is shown for an aqueous coating containing silica particles ($a = 200\,nm$) (S = sedimentation regime, E = evaporation regime, D = diffusion regime).

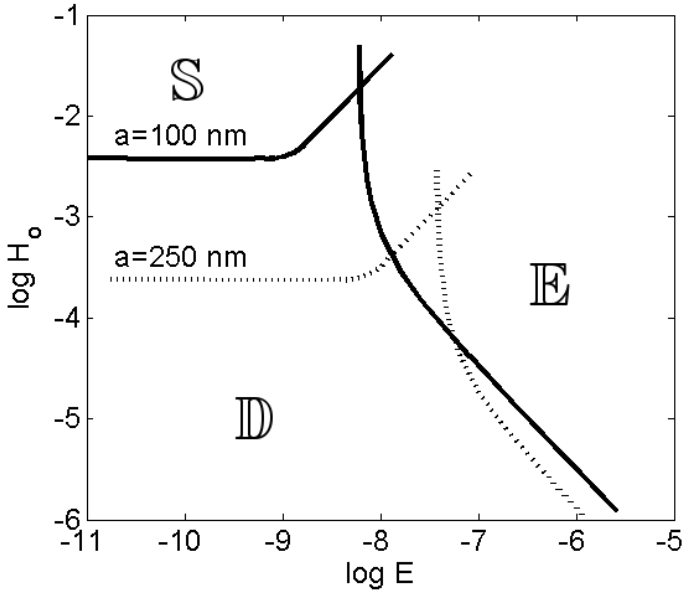

Figure 4.3. Drying regime map based on dimensional coordinates: initial coating thickness $H_0\,[m]$ and evaporation rate $E\,[m/s]$. The effect of silica particle size is shown for an aqueous dispersion with $\phi_0 = 0.2$ (S = sedimentation regime, E = evaporation regime, D = diffusion regime).

Drying regime maps – *log Pe vs. log* N_s

To create a universal map that is applicable to any coating system, evaporation (E), sedimentation (S) and diffusion (D) dominant regimes were found using the same method discussed previously and displayed with respect to the two dimensionless variables: Pe, and N_s. An example of a universal map for an initial particle volume fraction of 0.2 is shown in Figure 4.4. To find a position on the map, one calculates Pe and N_s (Equations 1.1 and 1.5) from measurable parameters: particle radius, a, particle density, ρ_p, liquid density, ρ, liquid viscosity, μ, and evaporation rate, E.

As demonstrated with the concentration profiles in Figure 4.1, the drying behavior can be split into two cases: high and low N_s, with a critical value of N_s ($N_{s,critical}$) that serves as the boundary between these two regimes. At low N_s, where $N_s \ll N_{s,critical}$, sedimentation is unimportant and evaporation and diffusion compete. Here, there is a critical Peclet number ($Pe_{critical}$) above which an evaporation-induced skin forms. At high N_s, where $N_s \gg N_{s,critical}$, evaporation is unimportant and sedimentation and diffusion compete. A critical sedimentation Peclet number is defined for this region ($Pe_{sed,critical}$).

$Pe_{sed,critical}$ varies with both N_s and Pe and marks the division between the diffusion dominated regime and the sedimentation dominated regime. Interestingly, the line for $Pe_{sed,critical}$ changes slope at $Pe_{critical}$, reflecting the increasing influence of evaporation in that region. A small overlap of the sedimentation and evaporation regions exist where both of these behaviors are predicted to be of consequence.

Figure 4.5 shows the effect of initial particle concentration on the drying regime map boundaries. Similar to Figures 4.2 and 4.3, as the initial volume fraction changes the critical values change, but the shape of drying regime map is retained. As discussed earlier, sedimentation and diffusion regimes are larger at smaller initial volume fraction. The effects of initial concentration on the boundaries of the drying map can be better understood by analytically solving limiting cases described by the critical dimensionless numbers.

At $N_{s,critical}$, where sedimentation and evaporation are balanced, a skin does not develop because the particle sedimentation rate beneath the air-water interface is exactly equal to the evaporation rate, or:

$$E \approx U(\xi = 1) = U_0 K(\phi_0) \tag{4.2}$$

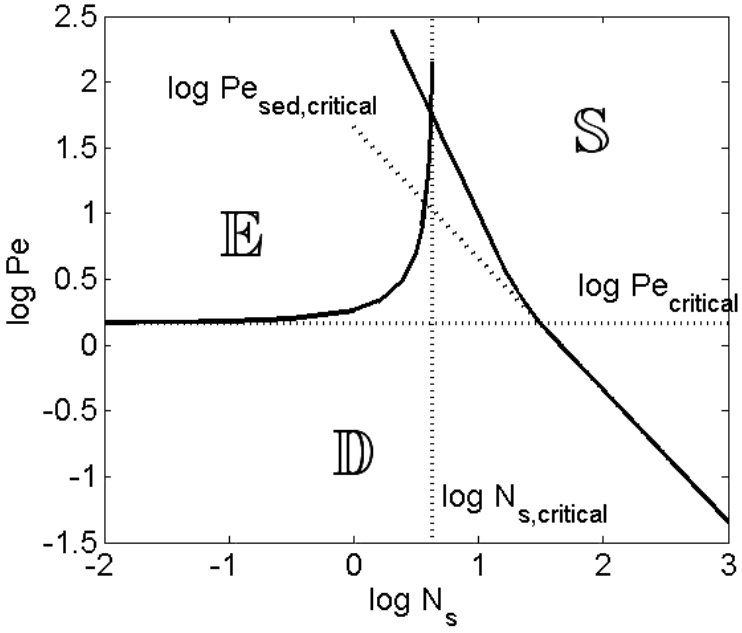

Figure 4.4. Drying regime map based on dimensionless coordinates: Peclet number (Pe) and sedimentation number (N_s). Evaporation (E), sedimentation (S), and diffusion (D) dominant regions are shown for a coating with ($\phi_0 = 0.2$). Critical values are also marked for limiting cases.

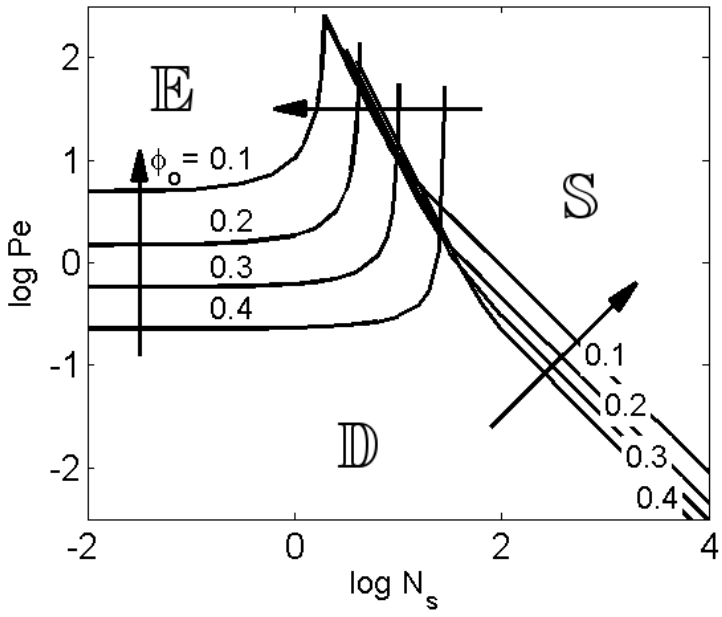

Figure 4.5. Effect of initial particle volume fraction on the drying regime map based on dimensionless coordinates.

$$N_{s,critical} = \frac{U_0}{E} = \frac{1}{K(\phi_0)} = \frac{1}{(1-\phi_0)^{6.55}}. \quad (4.3)$$

The predictions of Eq. 4.3 are compared with numerical results in Figure 4.6. This equation matches the numerical results well.

In the region of $Pe_{sed,critical}$, diffusion and sedimentation are of equal importance and evaporation does not have much effect. To determine when sedimentation and diffusion are in balance, the steady state conservation equation is solved with boundary conditions changed to reflect the lack of evaporation.

$$0 = \frac{\partial}{\partial \bar{y}}\left[N_s K(\phi)\phi + \frac{1}{Pe} K(\phi) \frac{d}{d\phi}\left[\phi Z(\phi)\right] \frac{\partial \phi}{\partial \bar{y}} \right] \quad (4.4)$$

$$N_s K(\phi)\phi + \frac{1}{Pe} K(\phi) \frac{d}{d\phi}\left[\phi Z(\phi)\right] \frac{\partial \phi}{\partial \bar{y}} = 0 \qquad at\ \bar{y} = 0\ or\ 1 \quad (4.5)$$

After a single integration of (4.5), the following is obtained:

$$\int_{\phi(0)}^{\phi(1)} \frac{-1}{PeN_s} \frac{\phi_{\max}}{(\phi_{\max} - \phi)^2} d\phi = \int_0^1 \phi d\bar{y} \quad (4.6)$$

Due to mass conservation, the right hand side of Eq. 4.6 equals ϕ_0 [Davis and Russel 1989]. Assuming negligible particle concentration at

the top surface of the coating ($\phi(1) = 0$), an expression for the volume fraction at the bottom is obtained.

$$\phi(\bar{y} = 0) = \frac{Pe_{sed}\phi_0\phi_{\max}}{1 + Pe_{sed}\phi_0} \tag{4.7}$$

At $Pe_{sed,critical}$, $\phi(\bar{y} = 0) = 0.9\phi_{max}$, so

$$Pe_{sed,\,critical} = \frac{9}{\phi_0}. \tag{4.8}$$

Figure 4.7 shows $Pe_{sed,critical}$ versus the initial volume fraction found numerically and approximated using Eq. 4.8. The calculation and the numerical result are almost the same.

In the case of $Pe_{critical}$, simple analytical solution was not obtained. However, interestingly, $Pe_{critical}$ has a power-law dependence on $\frac{(1-\phi_0)^{6.55}}{(\phi_{max}-\phi_0)^2}$, which is equal to $\frac{D(\phi_0)}{\phi_{max}D_0}$, within the range of the initial volume fraction solved by the numerical methods as follows:

$$Pe_{critical} = \left[\frac{\left(1-\phi_0\right)^{6.55}}{\left(\phi_{\max}-\phi_0\right)^2}\right]^3. \tag{4.9}$$

The power-law fitting using Eq. 4.9 is compared with the numerical

results in Figure 4.8. This equation matches the numerical results well.

The critical values are represented as the functions of only initial volume fraction in Eq. 4.3, 4.8 and 4.9. The dimensionless variables are normalized with their critical values as follows:

$$\frac{Pe}{Pe_{critical}} = \frac{6\pi\mu aEH_0\left(\phi_{\max}-\phi_0\right)^6}{kT\left(1-\phi_0\right)^{19.65}} \tag{4.10}$$

$$\frac{N_s}{N_{s,critical}} = \frac{2a^2g\left(1-\phi_0\right)^{6.55}\left(\rho_p-\rho\right)}{9\mu E} \tag{4.11}$$

$$\frac{Pe_{sed}}{Pe_{sed,\,critical}} = \frac{4\pi a^3H_0g\phi_0\left(\rho_p-\rho\right)}{27kT}. \tag{4.12}$$

At $Pe/Pe_{critical} > 1$ and $N_s/N_{s,critical} < 1$, an evaporation induced skin forms. Both the normalized Pe of Eq. 4.10 and the normalized N_s of Eq. 4.11 are strongly dependent on the initial volume fraction rather than other variables. Therefore, the formation of the skin is influenced greatly by the variation of the initial volume fraction. At $Pe_{sed}/Pe_{sed,critical} > 1$, a sediment develops. The normalized Pe_{sed} of Eq. 4.12 is proportional to the cube of the particle radius. Therefore, the formation of the sediment is most sensitive to the variation of the particle

size.

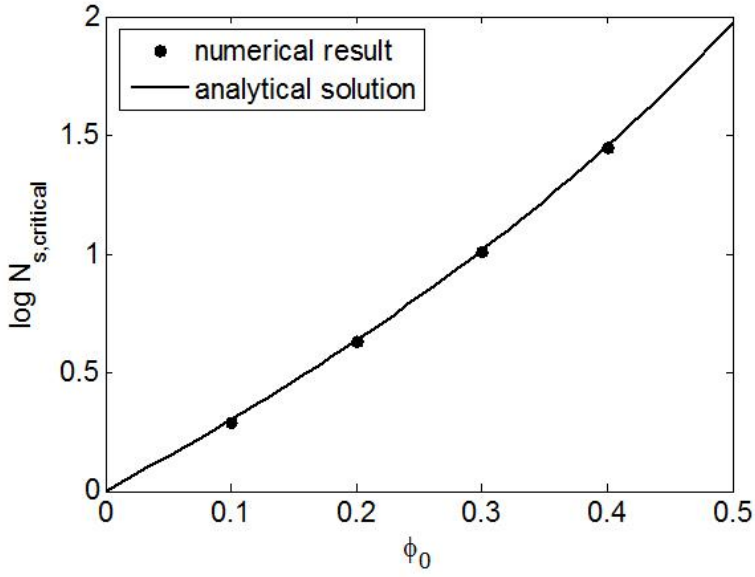

Figure 4.6. Dependence of $N_{s,critical}$ on the initial particle volume fraction found by numerically solving the full conservation equation and an analytical approximation (Eq. 4.3).

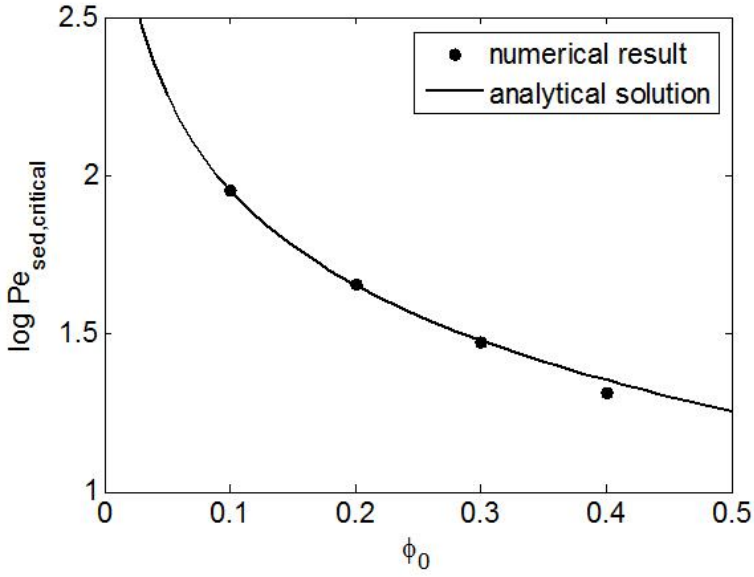

Figure 4.7. Dependence of $Pe_{sed,critical}$ on the initial particle volume fraction found by numerically solving the full conservation equation and an analytical approximation (Eq. 4.8).

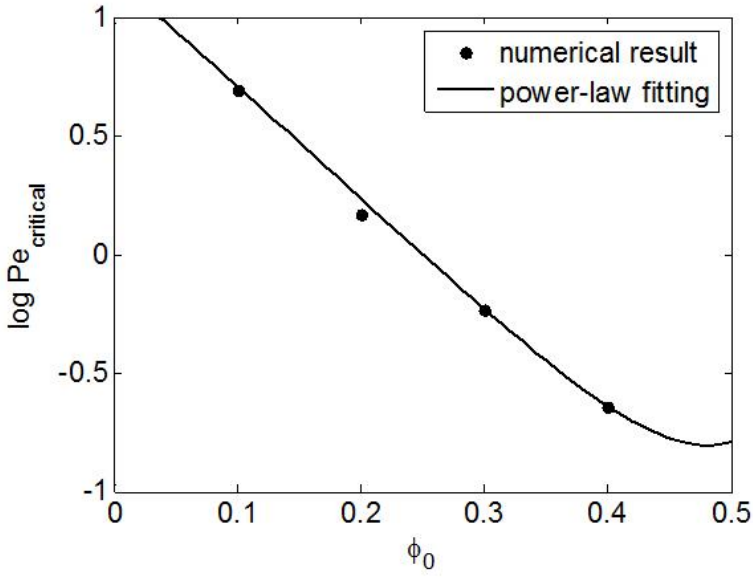

Figure 4.8. Dependence of $Pe_{critical}$ on the initial particle volume fraction found by numerically solving the full conservation equation and power-law fitting (Eq. 4.9).

4.1.3. Experimental results[1]

To demonstrate the effectiveness of the drying map to predict the microstructure development of a drying coating, cryoSEM was used to observe the microstructure of a model system under various drying conditions. Several conditions were investigated, as summarized in Table 4.1. These conditions explore all three regions of the drying map. Accumulation zones, also termed "close-packed region", were identified and noted if there was a noticeable concentration of particles at either the top or the bottom of the coating when the sample was halfway dry, or as close to this time point as possible. A representative selection of cryoSEM results are presented in Figures 4.10-4.13. The drying conditions for these samples are mapped for your convenience on Figure 4.9.

High evaporation rates and larger initial coating thicknesses tended to produce coatings that dried in the evaporation regime. CryoSEM images (Figure 4.10) show the evolution of a drying front that is growing in a coating dried in the evaporation regime. A layer of highly concentrated particles at the top of the coating grows with time, as marked by the white bar in the image. The particle concentration below this front stays

[1] Experimental results were produced by Christine M. Cardinal, Dept. of Chemical Engineering and Materials Science, University of Minnesota, Minneapolis, MN 55455

Table 4.1. Experimentally explored coating conditions.

a [nm]	ϕ_0	E $[\mu m/min]$	H_0 $[\mu m]$	ρ_p $[g/cm^3]$	Observed regime	$\log N_s$	$\log Pe$
200	0.1	7.8	183	1.9	Evaporation	-0.22	1.4
200	0.2	7.8	183	1.9	Evaporation	-0.22	1.4
91	0.2	2.0	250	1.9	Evaporation	-0.31	0.55
135	0.2	87	600	1.9	Evaporation	-1.6	2.7
200	0.2	62	250	1.9	Evaporation	-1.1	2.4
120	0.1	5.5	200	1.9	Evaporation	-0.51	1.0
50	0.1	5.5	200	2.2	Diffusion	-1.1	0.63
50	0.1	3.5	223	2.2	Diffusion	-0.95	0.48
500	0.1	22	130	2.2	Sediment / Evap	0.25	2.1
500	0.1	22	211	2.2	Sedimentation	0.25	2.3
500	0.1	2.0	250	2.2	Sedimentation	1.3	1.3
500	0.25	6.6	500	1.9	Sedimentation	0.65	2.1

approximately constant with time, as estimated visually from images. At the top surface of the coating some particles are ordered. Convective steering [Gasperino et al. 2008] and capillary forces at the free surface bring the particles together in an ordered crystal. This effect occurs because the particles are monodisperse. The crystal continues to grow when the time scale for particulate ordering is less than the addition speed of new particulates to the front. At $\bar{t} = 0.7$, the coating is fully consolidated. The top few layers of the final coating are polycrystalline with areas of close packing, whereas the bulk of the film is disordered. Large areas of particulate order may introduce some discrepancy with in the model, which assumes a random maximum packing fraction $\phi_{max} = 0.64$ instead of the packing fraction most commonly seen for colloidal crystals ($\phi_{max} = 0.74$). This model would overestimate the necessary Pe to form an ordered skin and overestimate the necessary N_s to form an ordered sediment. Since order was most often found only in small amounts through the depth of a skin and never in a sediment, this effect is assumed to be small in analyzing the given system.

If Pe is reduced from the evaporation regime by decreasing the drying rate or the size of the particles, diffusion plays a larger role in determining the particle distribution. The boundary between the skin and the bulk of

the coating was less distinct in coatings that were dried at lower Pe, near the evaporation/diffusion boundary in the drying regime map. Finally, in the diffusion regime, the concentration of particles remains fairly uniform with depth at any point in the drying, as shown in Figure 4.11.

In the sedimentation regime, large particles settled with a greater velocity than the evaporation velocity of the free surface, creating a region at the top of the coating that was depleted of particles (Figure 4.12). Below the particle-free zone was a zone of constant particle concentration, composed of free-falling particles. Near the sediment the transition zone is clear. As time progresses, the initial concentration zone decreases in length and the sediment grows until it includes all of the particles. Finally, the air-water interface recedes into the packing.

In the case where the particles in the coating sediment at a speed that is slower than the descent of the free surface, the model predicts that both a sediment and a skin can form simultaneously. This phenomena has been captured in Figure 4.13. An ordered particle packing appears at the top of the coating. This skin grows until it reaches the sediment near the substrate. Exploiting this phenomenon in more complicated coating systems may lead to inexpensive methods to produce novel coatings.

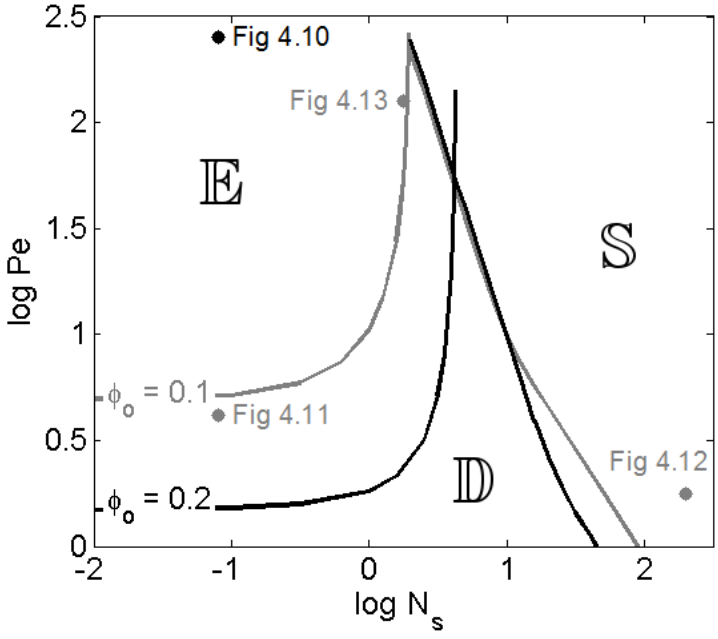

Figure 4.9. Drying regime map marking Pe and N_s corresponding to Figures 4.10-13. $\phi_0 = 0.1$ (grey) and $\phi_0 = 0.2$ (black).

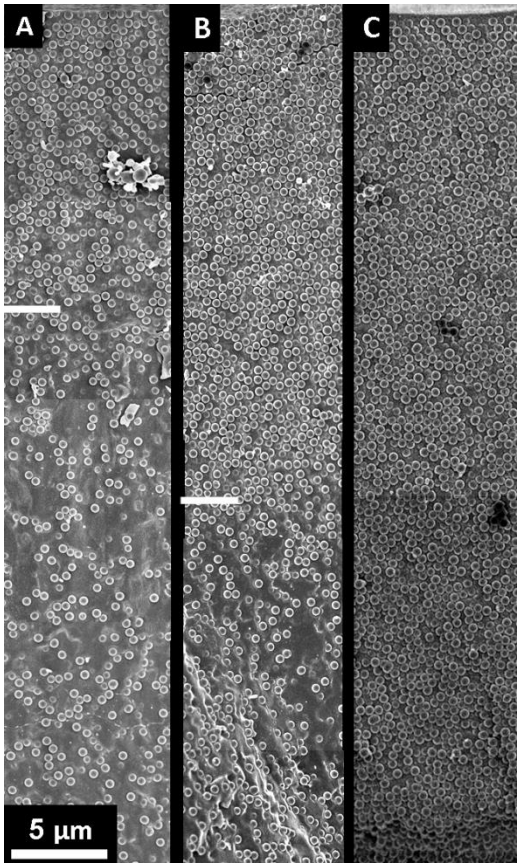

Figure 4.10. Cross-section cryoSEM images obtained at different time points showing evaporation dominance. Drying conditions were $\log Pe = 2.4,\ \log N_s = -1.1,\ \phi_0 = 0.2$. Dimensionless drying times and total coating thicknesses were (A) $\bar{t} = 0.3,\ H = 190\ \mu m$; (B) $\bar{t} = 0.4$; $H = 160\ \mu m$; (C) $\bar{t} = 0.7\ \ H = 70\ \mu m$. A white dash marks the edge of the consolidation front and the free surface is at the top of each image.

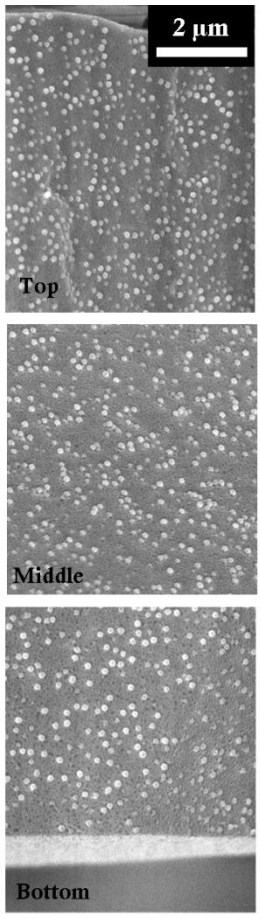

Figure 4.11. Cross-section cryoSEM image obtained at $\bar{t} = 0.4$ showing diffusion dominance. Images were from different depths in the coating, as shown. Drying conditions were $\log Pe = 0.62$, $\log N_s = -1.1$, $\phi_0 = 0.1$.

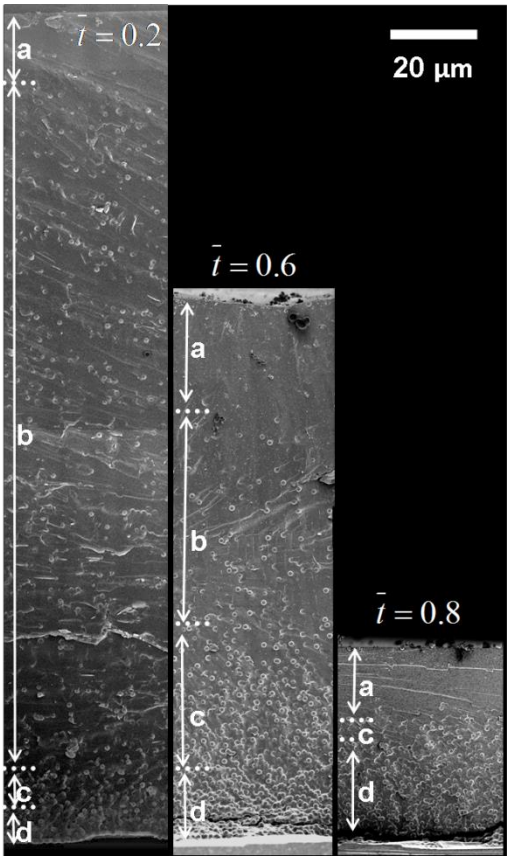

Figure 4.12. Cross-section cryoSEM images obtained at different times as indicated showing sedimentation dominance. Drying conditions were $\log Pe = 0.25,\ \log N_s = 2.3,\ \phi_0 = 0.1$. Sedimentation zones include (a) particle-free zone, (b) initial concentration zone, (c) transition zone and (d) sediment.

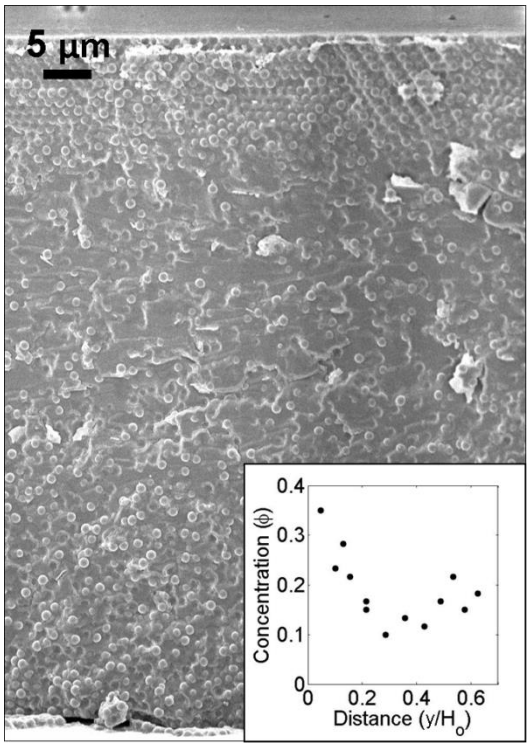

Figure 4.13. Cross-section cryoSEM image of a coating showing both sedimentation and evaporation dominance. $\bar{t} = 0.33$; $\log Pe = 0.25$; $\log N_s = 2.1$; $\phi_0 = 0.1$. The inset shows the volume fraction of particles as a function of depth in the coating as estimated from the image.

Conditions where sedimentation, diffusion and evaporation were observed experimentally are marked on the drying map in Figure 4.14. The experimental data match the model well, especially the delineation between diffusion and evaporation regimes. The sedimentation regime was found experimentally to occur at slightly lower N_s values than those predicted, corresponding to an underestimation of the sedimentation speed by the model. Lateral drying also influenced the particle distributions, especially at later drying times [Routh and Russel 1998; Deegan et al. 1997]. In this work, care was taken to minimize this effect so that results could be compared to the 1D model.

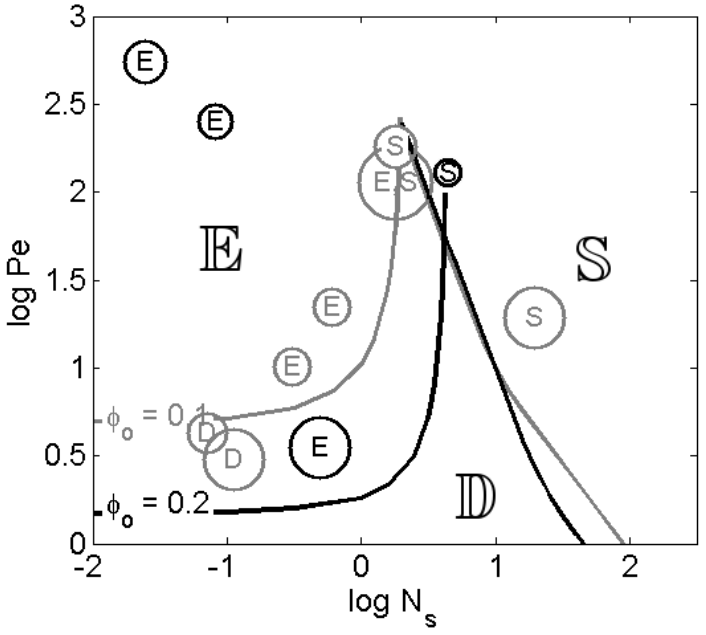

Figure 4.14. Drying map created from the theoretical model displaying points where evaporation (E), diffusion (D) and sedimentation (S) regimes were discovered through CryoSEM for $\phi_0 = 0.1$ (grey) and $\phi_0 = 0.2$ (black). Circle sizes denote the estimated magnitude of error.

Two particle system

To demonstrate how the understanding the drying behavior can be exploited to develop novel coatings, a two particle system was dried. A bimodal silica dispersion containing particles of $1\,\mu m$ in diameter and $200\,nm$ in diameter was prepared with an overall particle volume fraction of 0.2. The coating had an initial thickness of $400\,\mu m$ and was dried at $5\,\mu m/min$. The final result was a coating with a top layer entirely composed of smaller particles and a bottom layer of small particles dispersed between large particles (Figure 4.15).

The coating microstructure formation can be deduced from the drying regime map. Under the given conditions, the smaller silica particles were estimated to be in the evaporation regime and the larger particles were estimated to be in the sedimentation regime. Therefore, as drying occurred, the smaller particles accumulated at the free surface of the coating in a drying front whereas the larger particles sedimented towards the base. Those small particles that were not trapped in the consolidation front were scattered randomly throughout the sedimenting particles. Finally, enough water was lost from the coating that all particles were immobilized. The smaller particles that were trapped in the bottom of the coating were not

small enough to move between the fully consolidated larger particles. Otherwise, reorganization of the smaller particles could have continued after the larger particles had reached their final packing fraction, as observed elsewhere [Luo et al. 2007]. This type of coating could be a cost effective strategy to introduce a large particle filler into a film of expensive small particles without reducing the final quality of the product.

The application of the drying map to this example assumes that the sedimentation coefficient and compressibility factor are the same for a two particle system as for a one particle system. This assumption is not valid for particles that are very different in size. Therefore, more work is required to rigorously adapt the drying map to more complicated systems.

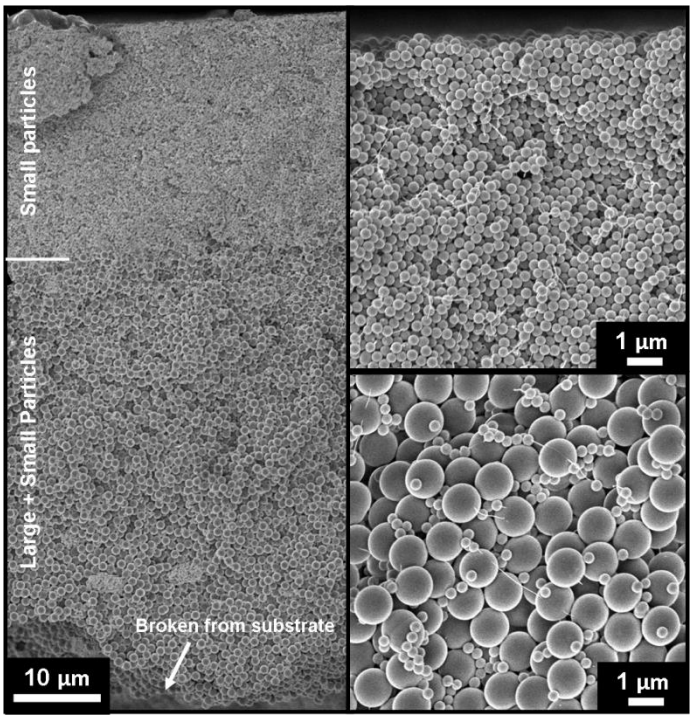

Figure 4.15. Cross-section image of a dried coating prepared from a bimodal aqueous silica dispersion. Top right: higher magnification image of top of coating. Bottom right: bottom of coating.

4.2. Convective assembly

4.2.1. Modeling results

The dimensionless length of the close-packed region and the dimensionless coating thickness are the functions of the three dimensionless variables: Ca, Ca_0 and ϕ_0. Comparing Eq. 2.34 and Eq. 2.35 with Eq. 1.7, the dimensionless coating thicknesses of the convective assembly and the Landau-Levich deposition have the same form, but are different only in the values of the exponents of the dimensionless variables. In the Landau-Levich equation, the dimensionless coating thickness is proportional to $Ca^{2/3}$ and ϕ_0. In the convective assembly, the dimensionless coating thickness is proportional to ${Ca_0}^{1}Ca^{-2}$ for the moving substrate, Eq. 2.34, or ${Ca_0}^{-1}$ for the static substrate, Eq. 2.35, and ${\phi_0}^{2}$. The Landau-Levich equation is applied when the close-packed region cannot be developed and the viscous stress mainly affects the dip coating process because Ca is large. The coating thickness of the Landau-Levich deposition increases as Ca increases. On the other hand, the convective assembly is applied when the close-packed region is formed on the substrate near the meniscus at the early stage of drying because Ca is small. As Ca increases, the coating thickness of the

convective assembly decreases because l_0 is decreased due to the increase in the pressure drop or the decrease in the maximum capillary pressure in the close-packed region.

Comparing Eq. 2.34 with Eq. 2.21 or Dimitrov and Nagayama's result, Eq. 2.22, l_0, which is a constant in Eq. 2.21 and Eq. 2.22, is replaced by l_0 from Eq. 2.33. And h_0 now depends not only on the coating conditions, E, u_s and ϕ_0, but also on the material properties of the suspension, a, γ and μ.

In Eq. 2.34, h_0 is shown as a function of the material properties (a, γ, μ) and the coating conditions (E, u_s, ϕ_0). When $u_s < E$ or $u_s = 0$, l_0 decreases with the increase in the pressure drop in the close-packed region as μ, E and u_s increase, and thus, h_0 decreases. When $u_s > E$, h_0 decreases as μ and u_s increase, but h_0 increases with E according to Eq. 2.34. This is because when $u_s > E$, the pressure drop is predominantly determined by u_s rather than E, and an increase in E increases the amount of the evaporation and enhances the particle packing at the particle packing front. As γ increases, the maximum capillary pressure increases, and l_0 as well as h_0 increases. As a increases, l_0 increases because the pressure drop is reduced by $1/a^2$ while the

maximum capillary pressure is reduced by $1/a$. Therefore, h_0 increases. As ϕ_0 increases, both l_0 and h_0 increase because more particles accumulate at the particle packing front.

4.2.2. Coating process regime maps

Using the modeling result for the static substrate, Eq. 2.35, a coating process regime map that predicts the coating thickness in terms of the dimensionless variables, ϕ_0 and Ca_0, was created shown in Figure 4.16. The coating thickness of the film formed by the convective assembly is discontinuous because the film has a structure consisting of the stacking of layers of hexagonally close-packed particles. Thus, the coating thickness was expressed as the number of layers, n, instead of the dimensionless coating thickness in the coating process regime map. The film has a monolayer when $\frac{h_0}{a} = 2$, a bilayer when $\frac{h_0}{a} = 3.633$ and n layers when $\frac{h_0}{a} = 2 + \frac{2\sqrt{6}}{3}(n-1)$. When n is an integer, the film with uniform coating thickness of n layers is formed because the growth rate of the film balances the difference in the velocities of substrate withdrawal and the descent of the surface of coating solution [Dimitrov and Nagayama 1996]. However, when n is not an integer, a difference between the growth rate of the film and the velocity of substrate withdrawal relative to the descent of surface exists. The meniscus between the surface of coating solution and the particle packing front changes with time, so uneven film [Brewer et al. 2011] with average coating thickness

of n layers or stripe pattern [Watanabe et al. 2009; Lee et al. 2009] appears. However, the mechanism of the film formation is not fully understood yet. The different shapes of the lines represent the coating conditions for the monolayer, bilayer, 10 layers and 100 layers, respectively. The slopes of the lines are $1/2$ because the dimensionless coating thickness is proportional to ${\phi_0}^2$ and ${Ca_0}^{-1}$. As ϕ_0 increases or Ca_0 decreases, h_0 increases.

In Eq. 2.34, the dimensionless coating thickness is expressed as the function of the three dimensionless variables, Ca, Ca_0 and ϕ_0. Because Ca_0 and Ca are not independent, a coating process regime map for the moving substrate was created in terms of Ca_0 and Ca while changing ϕ_0 shown in Figure 4.17. The thick lines represent the coating conditions for $\phi_0 = 0.01$ and the thin lines for $\phi_0 = 0.001$. The different shapes of the lines represent the coating conditions for the monolayer, bilayer, 10 layers and 100 layers. In the upper left corner of the map where Ca is smaller than Ca_0, the map was not drawn because $u_s < 0$. The slopes of the lines are 2 because the dimensionless coating thickness is proportional to Ca_0 and Ca^{-2}. If ϕ_0 is reduced, Ca needs to be reduced in order to form a film of the same coating thickness at a constant

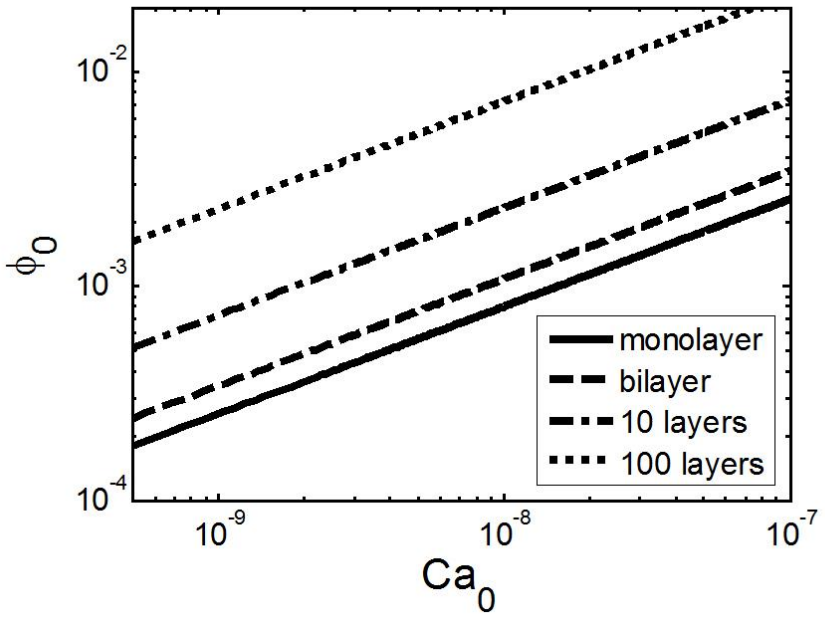

Figure 4.16. Coating process regime map for the static substrate ($u_s = 0$) based on the dimensionless coordinates: ϕ_0 and Ca_0, found by the modeling result of Eq. 2.35. The shape of the lines represents the coating thickness as indicated in the legend.

Ca_0. Therefore, the regime for $\phi_0 = 0.001$ lies on the left hand side of the regime for $\phi_0 = 0.01$, and h_0 increases as ϕ_0 increases for the same Ca_0 and Ca. Circle markers show the effect of E on h_0. The value of E increases as Ca_0 and Ca increase. As E increases, h_0 increases when $u_s > E$, but h_0 decreases when $u_s < E$. Triangle markers show the effect of γ or μ on h_0. The value of γ decreases or the value of μ increases as Ca_0 and Ca increase. As γ decreases or μ increases, h_0 decreases. Square markers show the effect of u_s on h_0. The value of u_s increases as Ca increases, and h_0 decreases as u_s increases.

Using Eq. 1.7 for the Landau-Levich deposition and Eq. 2.34 for the convective assembly, a coating process regime map in terms of the dimensionless variables, ϕ_0 and Ca, with a constant Ca_0 was created shown in Figure 4.18. The thick lines represent the coating conditions of the films being formed by the convective assembly and the thin lines by the Landau-Levich deposition. The different shapes of the lines represent the coating conditions for the monolayer, bilayer, 10 layers and 100 layers. Ca_0 was fixed at 1×10^{-9}. h_0 in Eq. 2.34 is nondimensionalized by a and the dimensionless coating thickness is independent of a. However,

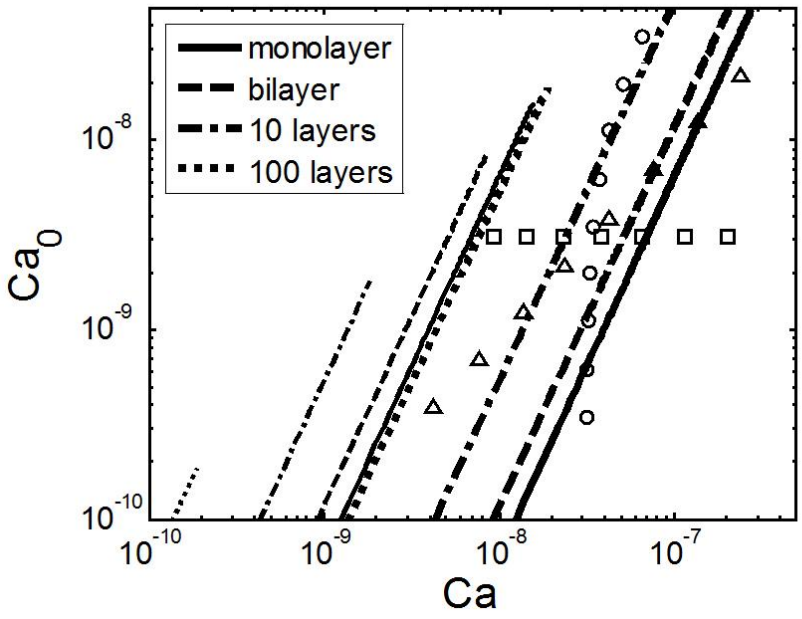

Figure 4.17. Coating process regime map for the moving substrate based on the dimensionless coordinates: Ca_0 and Ca, found by the modeling result of Eq. 2.34. The coating thicknesses are shown for the coatings with $\phi_0 = 0.01$ (thick lines) and $\phi_0 = 0.001$ (thin lines). The markers are depicted to illustrate the effects of material properties and coating conditions on the coating thickness: the effect of E on h_0 (○), the effect of γ or μ on h_0 (△) and the effect of u_s on h_0 (□).

$h_{LL,dry}$ in Eq. 1.7 is nondimensionalized by l_c and if it is nondimensionalized by a in order to fit in the same graph with Eq. 2.34, the dimensionless coating thickness will be inversely proportional to a. Therefore, a was fixed at $100\,nm$ only for Eq. 1.7. The coating thickness of the Landau-Levich deposition for an arbitrary a can be obtained by multiplying the coating thickness predicted by the coating process regime map by $\frac{100\,nm}{a}$. If $a = 200\,nm$ and the coating condition is located in the convective assembly regime (upper left part of the map), we can use the coating thickness predicted by the coating process regime map. However, if the coating condition is located in the Landau-Levich deposition regime (upper right part of the map), we need to multiply the coating thickness predicted by the coating process regime map by $\frac{100\,nm}{200\,nm} = 0.5$. The slopes of the thick lines in the convective assembly regime are 1 because the coating thickness is proportional to ${\phi_0}^2$ and Ca^{-2}, and the slopes of the thin lines in the Landau-Levich deposition regime are $-2/3$ because the coating thickness is proportional to ϕ_0 and $Ca^{2/3}$. At a small Ca, the film is formed by the convective assembly with the close-packed lattice structure, and the coating thickness decreases with Ca. If Ca continues to increase, the coating condition falls into the

Landau-Levich deposition regime. At the onset of the Landau-Levich deposition regime, where a transition between the convective assembly and the Landau-Levich deposition is realized, the close-packed monolayer can be developed [Brewer et al. 2011]. However, except at this transition, the film does not form a well-ordered structure as in the convective assembly, and the coating thickness increases as Ca increases. As ϕ_0 increases, the coating thickness increases both in the convective assembly regime and in the Landau-Levich deposition regime. Using this coating process regime map, one can predict the coating mechanism (convective assembly or Landau-Levich deposition), the degree of particle alignment (close-packed lattice structure or less ordered structure) and the coating thickness according to ϕ_0 and Ca under certain dip coating process conditions.

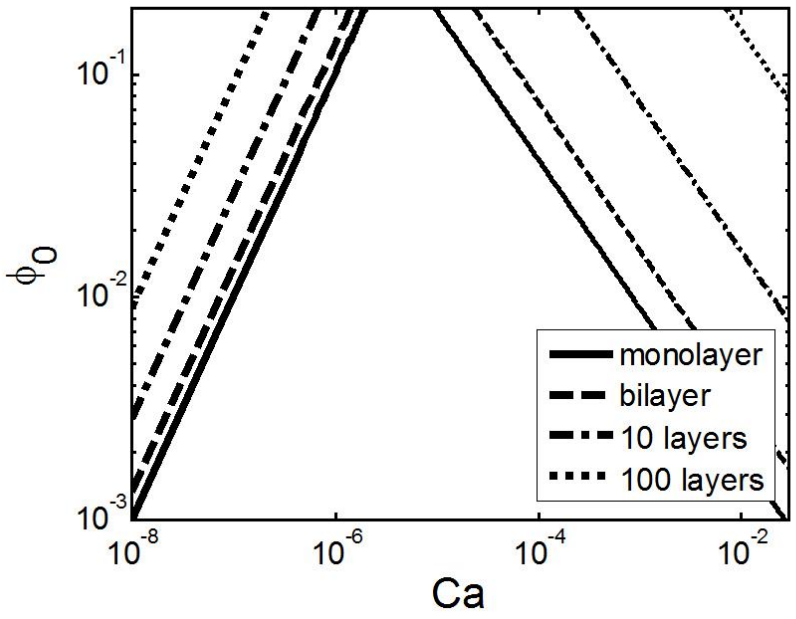

Figure 4.18. Coating process regime map, including the convective assembly regime found by Eq. 2.34 and the Landau-Levich deposition regime by Eq. 1.7, based on the dimensionless coordinates: ϕ_0 and Ca. Thick lines represent the coating thickness of films being formed by the convective assembly and thin lines by the Landau-Levich deposition. Ca_0 is fixed at 1×10^{-9}.

4.2.3. Experimental results

When $u_s = 0$, l_0 was measured under the various coating conditions with different ϕ_0 and E using a model system of monodisperse silica particles in alcohol. Table 4.2 shows the experimentally explored coating conditions and the average values of the measured l_0. A representative selection of the images of the close-packed region is presented in Figure 4.19. In the first four coating conditions l_0 increased with ϕ_0, and in the next, l_0 decreased with E.

Figure 4.20 shows the experimental results of the dependence of l_0 on ϕ_0. The error bars represent the standard deviations of l_0. The slope of the graph is 0.52 and l_0 was found to be proportional to ${\phi_0}^{0.52}$. According to Eq. 2.33, l_0 is proportional to ϕ_0 when $u_s = 0$. Both the experiments and modeling showed the trend of l_0 increasing with the increase in ϕ_0. However, in the experiments, the exponent of ϕ_0 was measured to be smaller than the modeling. Figure 4.21 shows the experimental results on the effects of E. The slope of the graph is -0.78 and l_0 was proportional to $E^{-0.78}$. In Eq. 2.33 of the modeling, l_0 is proportional to E^{-1} when $u_s = 0$. Both the experiments and modeling showed the trend of l_0 decreasing with the increase in E. However in the

experiments, the absolute value of the exponent of E was measured to be smaller than the model prediction. In the experiments on the effects of ϕ_0 and E, the absolute values of the exponents of both variables were measured to be smaller than the modeling. In addition, the difference between the experiments and the modeling was larger for the dependence on ϕ_0 than that on E.

One of the possible causes for the differences is that l_0 could be measured to be larger than the actual length in the experiments. In Figure 1.3, the particle packing front is located slightly above the surface of the coating solution due to the meniscus being formed in the position where the surface of the coating solution and the substrate meet. l_0 was determined experimentally by measuring the length of the transparent area between the two white areas shown in Figure 3.2 without observing the particles in the close-packed region directly. Therefore, l_0 could be measured larger than the actual length by including part of the meniscus. If l_0 was assumed to be measured $0.2 \times 10^{-3}\, m$ larger, l_0 could be recalculated to be proportional to ${\phi_0}^{0.61}$ and $E^{-0.87}$, which becomes more consistent with the modeling results. Furthermore, if we assume that l_0 was measured $0.43 \times 10^{-3}\, m$ larger, the experiments and the modeling would coincide on the effect of E on l_0. It is possible that a

Table 4.2. Experimentally explored coating conditions.

ϕ_0	$E\ [m/s]$	Ca_0	$l_0\ [m]$
0.001	9.7×10^{-8}	5.2×10^{-9}	0.8×10^{-3}
0.0025	9.7×10^{-8}	5.2×10^{-9}	1.4×10^{-3}
0.005	9.7×10^{-8}	5.2×10^{-9}	1.8×10^{-3}
0.01	9.7×10^{-8}	5.2×10^{-9}	2.7×10^{-3}
0.0025	3.6×10^{-8}	1.9×10^{-9}	2.9×10^{-3}
0.0025	6.1×10^{-8}	3.3×10^{-9}	2.0×10^{-3}
0.0025	9.7×10^{-8}	5.2×10^{-9}	1.4×10^{-3}

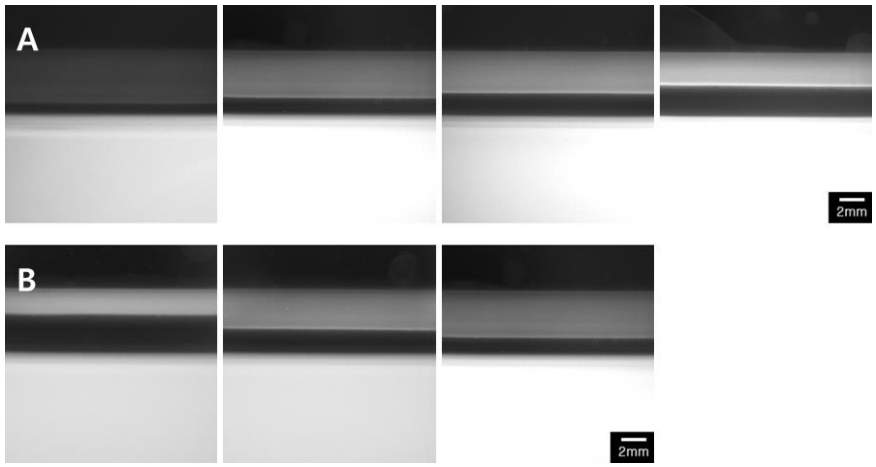

Figure 4.19. Images of the close-packed region at the various coating conditions: (A) $\phi_0 = 0.001$, $\phi_0 = 0.0025$, $\phi_0 = 0.005$ and $\phi_0 = 0.01$ with $E = 9.7 \times 10^{-8}\, m/s$; (B) $E = 3.6 \times 10^{-8}\, m/s$, $E = 6.1 \times 10^{-8}\, m/s$ and $E = 9.7 \times 10^{-8}\, m/s$ with $\phi_0 = 0.0025$.

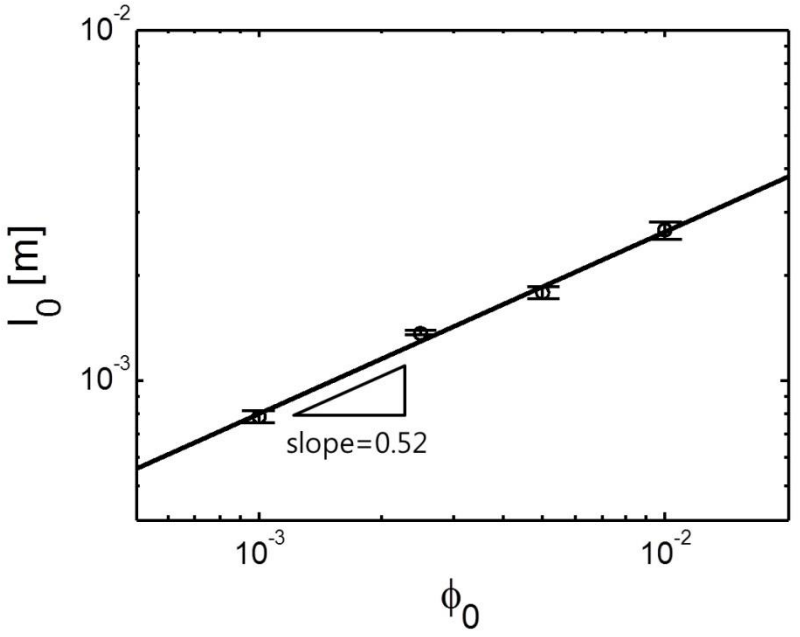

Figure 4.20. Dependence of the length of the close-packed region on the initial volume fraction. The slope of the graph represents the measured value of the exponent of ϕ_0.

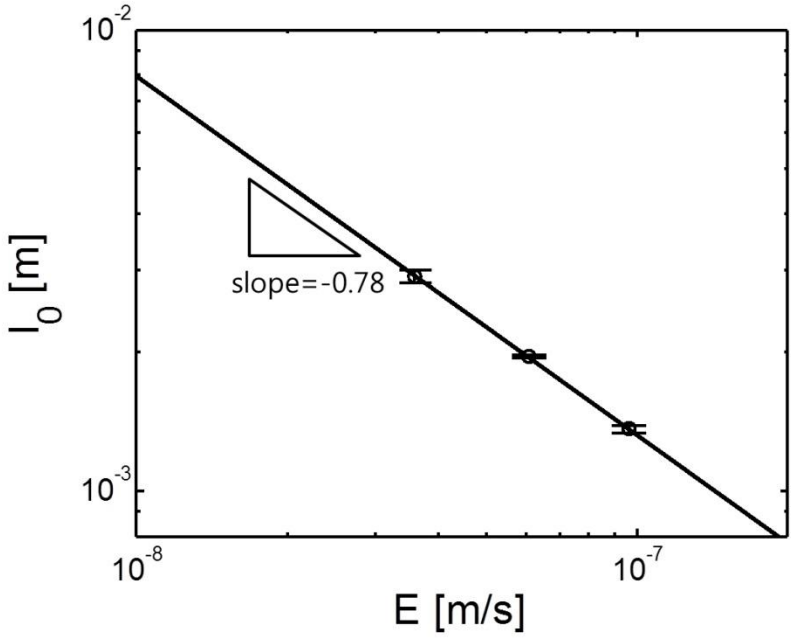

Figure 4.21. Dependence of the length of the close-packed region on the evaporation rate. The slope of the graph represents the measured value of the exponent of E.

greater part of the meniscus was included in determining l_0 for the coating solution with a low ϕ_0 because the coating solution with a low ϕ_0 is more transparent than a high ϕ_0. Therefore, the effect of ϕ_0 on l_0 could be measured to be much smaller.

If the pressure drop is proportional to the n^{th} power of the flow rate (n less than one), the modeling can predict the experimental results more closely. Darcy's law that was used to determine l_0 in the modeling describes the pressure drop when the Newtonian fluid goes through the packed bed composed of the monodisperse hard spheres. Because the model system used in the experiments was not a perfect monodisperse hard sphere, by assuming that the pressure drop in the close-packed region was proportional to the n^{th} power of the flow rate, l_0 could be re-derived. When $u_s = 0$, Darcy's law was modified according to the assumptions above.

$$\frac{\partial p}{\partial x} = -\frac{\mu}{k_{p,n}(a)}\left(1-\phi_m\right)^n \bar{u}_x^{\,n}, \tag{4.13}$$

where $k_{p,n}$ is the permeability of the modified Darcy's law. Because k_p from Eq. 2.27 is the function of a, $k_{p,n}$ was also assumed to be the function of a. The dependence of the permeability on ϕ_m was not

considered because ϕ_m is a constant. By substituting $u_s = 0$ into Eq. 2.29, $l_p = l_0$ was recovered. By equating the amount of the pressure drop calculated by integrating Eq. 4.13 from $x = x_0$ to $x = x_0 + l_0$ after utilizing $\bar{u}_x(x)$ from Eq. 2.26 and the maximum capillary pressure, the following equation was obtained.

$$-\int_{x_0}^{x_0+l_0} -\frac{\mu(1-\phi_m)^n}{k_{p,n}(a)}\left\{\frac{E(\phi_m-\phi_0)}{(1-\phi_m)\phi_0}\left[1-\frac{(x-x_0)}{l_0}\right]\right\}^n dx = \frac{10\gamma}{a} \quad (4.14)$$

After solving l_0 in Eq. 4.14 and assuming ϕ_0 is small, l_0 was derived as

$$l_0 = \frac{\gamma f_n(a)}{\mu}\frac{{\phi_0}^n}{E^n}, \quad (4.15)$$

where $f_n(a) = \frac{10(n+1)}{a{\phi_m}^n}k_{p,n}(a)$. Inserting l_0 from Eq. 4.15 into Eq. 2.21, h_0 was obtained.

$$h_0 = \frac{1.35\gamma f_n(a)}{\mu}\frac{{\phi_0}^{n+1}}{E^n} \quad (4.16)$$

In Eq. 4.15, l_0 is proportional to ${\phi_0}^n$ and E^{-n}. If $n = 0.52$, the modeling results can explain the experimental results of the effect of ϕ_0.

And if $n = 0.78$, the modeling can describe well the experimental results of the effect of E.

V. Conclusions

The properties and performances of the coatings depend on the microstructure, and it is important to understand the microstructural change during drying which can be characterized by the particle distribution, the degree of alignment and the coating thickness. In general, as a particulate coating dries, the close-packed region is formed from the boundary of the coating. The capillary pressure of the meniscus in the close-packed region and the fluid flow into or through the close-packed region have a strong influence on the film formation. Therefore, predicting the formation of the close-packed region and understanding the role of the close-packed region give useful information on the microstructure such as the degree of alignment and the coating thickness as well as the particle distribution. Two particulate coating methods, drying of colloidal films and convective assembly, were investigated by modeling the formation of the close-packed region. Furthermore, the coating regime maps that predict the microstructural change depending on the coating conditions in terms of the dimensionless variables were

created. The model predictions were validated by the experiments.

To investigate the drying of colloidal films, the nonlinear 1D conservation equation with concentration dependent diffusion and sedimentation coefficients was solved for the particle concentration profiles at different time points for various drying conditions. This gave a picture of the particle distribution before air invades into the particle packing. From this data, the drying regime maps, which predict the presence of the close-packed region (particle surface accumulation or sediment) based on two dimensionless numbers, Pe and N_s, were developed. It was then demonstrated that certain limiting cases of the drying regime map could be calculated analytically. The particle distribution during drying of a model system comprised of monodisperse silica particles in water was observed using cryoSEM. Particle size and evaporation rates were altered to access various domains of the drying regime map. There was a good agreement between experimental observations and model predictions.

To analyze the convective assembly, the length of the close-packed region and the coating thickness were predicted by combining Darcy's law with the particle and solvent balance equations in the close-packed region.

The dimensionless length of the close-packed region and the dimensionless coating thickness were found to be the functions of only three dimensionless variables: Ca, Ca_0 and ϕ_0. From the modeling results, the coating process regime maps that predict the dimensionless coating thickness for a given coating condition in terms of the dimensionless variables were created. By using the coating process regime map which combines the Landau-Levich deposition regime altogether, one can predict the mechanism (convective assembly or Landau-Levich deposition), the degree of particle alignment and the coating thickness in terms of Ca and ϕ_0 under an arbitrary dip coating process. In addition, the effects of the initial volume fraction and the evaporation rate on the length of the close-packed region were observed experimentally to validate the model predictions. The experiments firmly supported the model predictions.

It is hoped that this work will provide greater understanding of the particulate coating process and it can be used to design coating conditions to produce the desired microstructures of particulate coatings.

Nomenclature

a: particle radius

β: ratio between the velocity of a particle in solution and the fluid velocity

Ca: capillary number

Ca_0: capillary number when the drawing speed is zero

D: particle mutual diffusion coefficient

D_0: Stokes-Einstein diffusion coefficient

E: evaporation rate (in units of distance per time)

g: gravitational acceleration

γ: solvent surface tension

h_0: coating thickness of the film developed by the convective assembly

$h_{LL,dry}$: dry coating thickness of the film developed by the Landau-Levich deposition

H_0: initial coating thickness of the colloidal film

k: Boltzmann constant

k_p: permeability

$k_{p,n}$: permeability of the modified Darcy's law

K: sedimentation coefficient

l_0: length of the close-packed region

l_c: capillary length

l_p: length between the particle packing front and the position where the pressure gradient is zero in the close-packed region

μ: solvent viscosity

n: the number of layers of hexagonally close-packed particles

n: index of the modified Darcy's law

N_s: sedimentation number

$N_{s,critical}$: critical sedimentation number

p: pressure

p_c: capillary pressure

Pe: Peclet number

$Pe_{critical}$: critical Peclet number

Pe_{sed}: sedimentation Peclet number

$Pe_{sed,critical}$: critical sedimentation Peclet number

ϕ: particle volume fraction

ϕ_0: initial particle volume fraction

ϕ_m: particle volume fraction of the close-packed lattice structure

ϕ_{max}: maximum packing fraction

ϕ_r: particle volume fraction of the random close packing structure

Re: Reynolds number

ρ: solvent density

ρ_p: particle density

t: time

$\bar{t}$: dimensionless time

$\bar{t}_m$: dimensionless time when the entire coating is packed with maximum packing

T: temperature

τ: dimensionless time of the shrinking coordinate system

u_s: substrate drawing speed

$\bar{u}_x$: flow rate of the fluid in the *x*-direction averaged over the film thickness

U: sedimentation velocity

U_0: Stokes settling velocity

$v_c^{(n)}$: growth rate of the n-layer array

V_D: velocity of a Brownian particle

w: width of the substrate

x: Cartesian coordinate parallel to the substrate

x_0: position of the particle packing front

x_0^-: position beneath the particle packing front

x_0^+: position above the particle packing front

ξ: dimensionless *y* coordinate of the shrinking coordinate system

y: Cartesian coordinate normal to the substrate

$\bar{y}$: dimensionless *y* coordinate

Z: compressibility factor

Bibliography

In alphabetical order by first author,

Ackerson, B. J.; Paulin, S.; Johnson, B.; van Megen, W.; Underwood, S., Crystallization by settling in suspensions of hard spheres. *Physical Review E* **1999**, 59 (6), 6903.

Berteloot, G.; Daerr, A.; Lequeux, F.; Limat, L., Dip coating with colloids and evaporation. Chemical Engineering and Processing: *Process Intensification* **2012**, 68 (0), 69-73.

Bogush, G.; Tracy, M.; Zukoski, C., Preparation of monodisperse silica particles: control of size and mass fraction. *Journal of Non-Crystalline Solids* **1988**, 104 (1), 95-106.

Brewer, D. D.; Allen, J.; Miller, M. R.; de Santos, J. M.; Kumar, S.; Norris, D. J.; Tsapatsis, M.; Scriven, L., Mechanistic principles of colloidal crystal growth by evaporation-induced convective steering. *Langmuir* **2008**, 24 (23), 13683-13693.

Brewer, D. D.; Shibuta, T.; Francis, L.; Kumar, S.; Tsapatsis, M., Coating process regimes in particulate film production by forced-convection-assisted drag-out. *Langmuir* **2011**, 27 (18), 11660-70.

Brown, G. L., Formation of films from polymer dispersions. *Journal of Polymer science* **1956**, 22 (102), 423-434.

Buscall, R.; White, L. R., The consolidation of concentrated suspensions. Part 1.-The theory of sedimentation. *Journal of the Chemical Society, Faraday Transactions 1: Physical Chemistry in Condensed Phases* **1987**, 83 (3), 873-891.

Cairncross, R. A.; Francis, L. F.; Scriven, L. E., Predicting drying in coatings that react and gel: Drying regime maps. *AIChE Journal* **1996**, 42 (1), 55-67.

Carman, P., Fluid flow through granular beds. *Transactions-Institution of Chemical Engineeres* **1937**, 15, 150-166.

Chapman, D. In Coating structure effects on ink-jet print quality, COATING CONFERENCE-TAPPI, TAPPI PRESS: **1997**; pp 73-94.

Ciampi, E.; Goerke, U.; Keddie, J.; McDonald, P., Lateral transport of water during drying of alkyd emulsions. *Langmuir* **2000**, 16 (3), 1057-1065.

Davis, K. E.; Russel, W. B.; Glantschnig, W. J., Settling suspensions of colloidal silica: observations and X-ray measurements. *Journal of the Chemical Society, Faraday Transactions* **1991**, 87 (3), 411-424.

Davis, K.; Russel, W. B., An asymptotic description of transient settling and ultrafiltration of colloidal dispersions. *Physics of Fluids A: Fluid Dynamics* **1989**, 1, 82.

Davis, R. H.; Birdsell, K. H., Hindered settling of semidilute monodisperse and polydisperse suspensions. *AIChE Journal* **1988**, 34 (1), 123-129.

Deegan, R. D.; Bakajin, O.; Dupont, T. F.; Huber, G.; Nagel, S. R.; Witten, T. A., Capillary flow as the cause of ring stains from dried liquid drops. *Nature* **1997**, 389 (6653), 827-829.

Deegan, R. D.; Bakajin, O.; Dupont, T. F.; Huber, G.; Nagel, S. R.; Witten, T. A., Contact line deposits in an evaporating drop. *Physical Review E* **2000**, 62 (1), 756.

Dimitrov, A. S.; Nagayama, K., Continuous convective assembling of fine particles into two-dimensional arrays on solid surfaces. *Langmuir* **1996**, 12 (5), 1303-1311.

Dixit, H. N.; Homsy, G., The elastic Landau–Levich problem. *Journal of Fluid Mechanics* **2013**, 732, 5-28.

Dominko, R.; Gaberscek, M.; Drofenik, J.; Bele, M.; Pejovnik, S.; Jamnik, J., The role of carbon black distribution in cathodes for Li ion batteries. *Journal of power sources* **2003**, 119, 770-773.

Ekanayake, P.; Doughty, P.; Keddie, J.; McDonald, P., Experimental tests of scaling predictions of the spatial distribution of particles during the drying of colloidal films. *Magnetic Resonance Imaging* **2007**, 25 (4), 557.

Fustin, C.-A.; Glasser, G.; Spiess, H. W.; Jonas, U., Parameters influencing the templated growth of colloidal crystals on chemically patterned surfaces. *Langmuir* **2004**, 20 (21), 9114-9123.

Gasperino, D.; Meng, L.; Norris, D. J.; Derby, J. J., The role of fluid flow and convective steering during the assembly of colloidal crystals. *Journal of Crystal Growth* **2008**, 310 (1), 131-139.

Gasperino, D.; Meng, L.; Norris, D. J.; Derby, J. J., The role of fluid flow and convective steering during the assembly of colloidal crystals. *Journal of Crystal Growth* **2008**, 310 (1), 131-139.

Gorce, J. P.; Bovey, D.; McDonald, P. J.; Palasz, P.; Taylor, D.; Keddie, J. L., Vertical water distribution during the drying of polymer films cast from aqueous emulsions. *Eur. Phys. J. E* **2002**, 8 (4), 421-429.

Hattori, H., Anti-Reflection Surface with Particle Coating Deposited by Electrostatic Attraction. *Advanced Materials* **2001**, 13 (1), 51-54.

Holtz, J. H.; Asher, S. A., Polymerized colloidal crystal hydrogel films as intelligent chemical sensing materials. *Nature* **1997**, 389 (6653), 829-832.

Im, S. H.; Kim, M. H.; Park, O. O., Thickness control of colloidal crystals with a substrate dipped at a tilted angle into a colloidal suspension. *Chemistry of Materials* **2003**, 15 (9), 1797-1802.

Jiang, P.; Bertone, J.; Hwang, K.; Colvin, V., Single-crystal colloidal multilayers of controlled thickness. *Chemistry of Materials* **1999**, 11 (8), 2132-2140.

Keddie, J.; Routh, A. F., Fundamentals of latex film formation: processes and properties. Springer: **2010**.

Kynch, G. J., A theory of sedimentation. *Transactions of the Faraday Society* **1952**, 48 (0), 166-176.

Landau, L.; Levich, B., Dragging of a liquid by a moving plate. *Acta Physicochimica U.R.S.S.* **1942**, 17, 42-54.

Le Berre, M.; Chen, Y.; Baigl, D., From convective assembly to Landau-Levich deposition of multilayered phospholipid films of controlled thickness. *Langmuir* **2009**, 25 (5), 2554-7.

Lee, J. A.; Reibel, K.; Snyder, M. A.; Scriven, L.; Tsapatsis, M., Geometric model describing the banded morphology of particle films formed by convective assembly. *ChemPhysChem* **2009**, 10, 2116-2122.

Li, G.; Pickup, P. G., Ionic Conductivity of PEMFC Electrodes: Effect of Nafion Loading. *Journal of The Electrochemical Society* **2003**, 150 (11), C745-C752.

Luo, H.; Cardinal, C. M.; Scriven, L. E.; Francis, L. F., Ceramic Nanoparticle/Monodisperse Latex Coatings. *Langmuir* **2008**, 24 (10), 5552-5561.

Luo, H.; Scriven, L.; Francis, L. F., Cryo-SEM studies of latex/ceramic nanoparticle coating microstructure development. *Journal of colloid and interface science* **2007**, 316 (2), 500-509.

Ma, Y.; Davis, H.; Scriven, L., Microstructure development in drying latex coatings. *Progress in organic coatings* **2005**, 52 (1), 46-62.

Maki, K. L.; Kumar, S., Fast evaporation of spreading droplets of colloidal suspensions. *Langmuir* **2011**, 27 (18), 11347-11363.

Marlow, F.; Sharifi, P.; Brinkmann, R.; Mendive, C., Opals: status and prospects. *Angewandte Chemie International Edition* **2009**, 48 (34), 6212-6233.

Meng, L.; Wei, H.; Nagel, A.; Wiley, B. J.; Scriven, L. E.; Norris, D. J., The role of thickness transitions in convective assembly. *Nano letters* **2006**, 6 (10), 2249-53.

O'Regan, B.; Gratzel, M., A low-cost, high-efficiency solar cell based on dye-sensitized colloidal TiO_2 Films. *Nature* **1991**, 353, 737-740.

Ouriemi, M.; Homsy, G. M., Experimental study of the effect of surface-absorbed hydrophobic particles on the Landau-Levich law. *Physics of Fluids* **2013**, 25 (8), 082111.

Routh, A. F.; Russel, W. B., A Process Model for Latex Film Formation: Limiting Regimes for Individual Driving Forces. *Langmuir* **1999**, 15 (22), 7762-7773.

Routh, A. F.; Russel, W. B., Horizontal drying fronts during solvent evaporation from latex films. *AIChE Journal* **1998**, 44 (9), 2088-2098.

Routh, A. F.; Zimmerman, W. B., Distribution of particles during solvent evaporation from films. *Chemical Engineering Science* **2004**, 59 (14), 2961-2968.

Russel, W. B., On the dynamics of the disorder-order transition. *Phase Transitions: A Multinational Journal* **1990**, 21 (2-4), 127-137.

Russel, W. B.; Saville, D. A.; Schowalter, W. R., Colloidal dispersions. Cambridge University Press: **1989**.

Salamanca, J.; Ciampi, E.; Faux, D.; Glover, P.; McDonald, P.; Routh, A.; Peters, A.; Satguru, R.; Keddie, J., Lateral drying in thick films of waterborne colloidal particles. *Langmuir* **2001**, 17 (11), 3202-3207.

Sarkar, A.; Tirumkudulu, M. S., Consolidation of Charged Colloids during Drying. *Langmuir* **2009**, 25 (9), 4945-4953.

Schabel, W.; Ludwig, I.; Kind, M., Measurements of Concentration Profiles in Polymeric Solvent Coatings by Means of an Inverse Confocal Micro Raman Spectrometer-Initial Results. *Drying Technology* **2004**, 22 (1-2), 285-294.

Sun, S.; Murray, C.; Weller, D.; Folks, L.; Moser, A., Monodisperse FePt nanoparticles and ferromagnetic FePt nanocrystal superlattices. *Science* **2000**, 287 (5460), 1989-1992.

Stöber, W.; Fink, A.; Bohn, E., Controlled growth of monodisperse silica spheres in the micron size range. *Journal of colloid and interface science* **1968**, 26 (1), 62-69.

van Duijneveldt, J. S.; Dhont, J. K. G.; Lekkerkerker, H. N. W., Expansion and crystallization of a sediment of charged colloidal spheres. *The Journal of Chemical Physics* **1993**, 99 (9), 6941-6949.

Vlasov, Y. A.; Bo, X.-Z.; Sturm, J. C.; Norris, D. J., On-chip natural assembly of silicon photonic bandgap crystals. *Nature* **2001**, 414 (6861), 289-293.

Wang, W.; Gu, B.; Liang, L.; Hamilton, W., Fabrication of Two- and Three-Dimensional Silica Nanocolloidal Particle Arrays. *The Journal of Physical Chemistry B* **2003**, 107 (15), 3400-3404.

Watanabe, S.; Inukai, K.; Mizuta, S.; Miyahara, M. T., Mechanism for Stripe Pattern Formation on Hydrophilic Surfaces by Using Convective Self-Assembly. *Langmuir* **2009**, 25 (13), 7287-7295.

Xia, Y.; Gates, B.; Yin, Y.; Lu, Y., Monodispersed colloidal spheres: old materials with new applications. *Advanced Materials* **2000**, 12 (10), 693-713.

Yiantsios, S. G.; Higgins, B. G., Marangoni flows during drying of colloidal films. *Physics of Fluids* **200**6, 18 (8), 082103-082111.

Zhou, Z.; Zhao, X., Flow-controlled vertical deposition method for the fabrication of photonic crystals. *Langmuir* **2004**, 20 (4), 1524-1526.

국문 초록

입자계 코팅은 페인트, 접착제, 종이, 무반사 코팅, 배터리, 연료전지, 광학소자, 저장매체 등 수 많은 산업에서 광범위하게 사용된다. 입자계 코팅은 입자와 용매, 고분자 바인더, 첨가제 등으로 구성된다. 입자계 코팅의 구성 요소가 동일하더라도 건조 후 형성된 필름의 미세구조가 다르면 최종 제품의 물성과 성능에 차이를 보이게 된다. 따라서 건조가 일어나는 동안 입자의 분포와 정렬 정도, 코팅 두께 등을 특정 지음으로써 미세구조를 이해하고 예측하는 것이 중요하다. 일반적으로 입자계 코팅이 건조될 때 용매가 증발함에 따라 코팅의 경계에서부터 close-packed region이 형성된다. Close-packed region은 밀집된 입자들 사이의 공간이 용매로 채워져 있는 부분을 말한다. Close-packed region에서 용매의 메니스커스에 의한 모세관력과 close-packed region을 지나가는 용매의 유동은 입자계 코팅의 필름 형성 과정에 많은 영향을 미친다. 따라서 건조 중 close-packed region의 형성을 예측하고 그 역할을 이해하는 것은 입자의 분포뿐만 아니라 입자의 정렬 정도와 코팅 두께와 같은 필름의 미세구조를 예측하는데 있어서 유용하게 사용될 수 있다.

본 연구에서는 입자계 필름의 건조와 대류자가조립 공정이라는 두 가지 입자계 코팅 방법에 대하여 close-packed region의 형성 과정을 모델링 하였고, 코팅 공정 조건에 따른 필름의 미세

구조의 변화를 예측하는데 이용할 수 있는 무차원 변수를 축으로 하는 코팅 영역 지도를 완성하였다. 입자계 필름의 건조에 관한 연구에서는 입자계 건조 중 증발과 확산, 침전이 close-packed region의 형성에 미치는 영향을 보존방정식을 풀어서 모델링 하였다. 이 결과로부터 주어진 건조 조건에서 증발과 확산, 침전 중 어떠한 현상이 더 지배적인가를 예측할 수 있는 무차원 변수인 Pe와 N_s를 축으로 하는 건조 영역 지도를 완성하였다. 물에 분산된 균일한 실리카 입자를 사용하여 다양한 건조 조건에서 건조 중 코팅 두께 방향의 입자의 분포를 관찰하였고, 모델링과 실험 결과가 일치함을 확인하였다. 또한 대류자가조립 공정에 관한 연구에서는 입자 결정 필름을 형성하는데 있어서 close-packed region의 역할에 대하여 설명하였고, 물질수지식을 풀어서 close-packed region의 길이와 코팅 두께를 예측하였다. 무차원화된 close-packed region의 길이와 코팅 두께는 세 가지 무차원 변수인 Ca와 Ca_0, 초기 입자의 농도의 함수로 표현되었다. 이 결과로부터 임의의 대류자가조립 공정의 코팅 두께를 예측하는데 이용할 수 있는 코팅 공정 영역 지도를 완성하였다. 또한 알코올에 분산된 균일한 실리카 입자를 모델 시스템으로 사용하여 코팅 공정 조건이 close-packed region의 길이에 미치는 영향을 관찰하였고, 모델링과 실험 결과가 일치함을 확인하였다.

주요어: 입자계 코팅, 입자계 필름의 건조, 대류자가조립, 코팅

영역 지도, 건조 영역 지도

학번: 2006-21386